ISSN 1674-1056
http://cpb.iphy.ac.cn
http://iopscience.iop.org/cpb
中国物理 B
Chinese Physics
中国物理 Chinese Physics B

Fundamental and progress of Bi_2Te_3-based thermoelectric materials

Min Hong(洪敏), Zhi-Gang Chen(陈志刚), Jin Zou(邹进)
Citation: Chin. Phys. B . 2018, 27(4): 048403. **doi:** 10.1088/1674-1056/27/4/048403

Journal homepage: http://cpb.iphy.ac.cn; http://iopscience.iop.org/cpb

What follows is a list of articles you may be interested in

Enhancement of thermoelectric properties of $SrTiO_3$/LaNb-$SrTiO_3$ composite by different doping levels

Ke-Xian Wang(王柯鲜), Jun Wang(王俊), Yan Li(李艳), Tao Zou(邹涛), Xiao-Huan Wang(王晓欢), Jian-Bo Li(李建波), Zheng Cao(曹正), Wen-Jing Shi(师文静), Xinba Yaer(新巴雅尔)
Chin. Phys. B . 2018, 27(4): 048401. **doi:** 10.1088/1674-1056/27/4/048401

Synthesis and thermoelectric properties of Nd-single filled p-type skutterudites

Hong Wu(吴宏), Nusrat Shaheen, Heng-Quan Yan(杨恒全), Kun-Ling Peng(彭坤岭), Xing-Chen Shen(沈星辰), Guo-Yu Wang(王国玉), Xu Lu(卢旭), Xiao-Yuan Zhou(周小元)
Chin. Phys. B . 2018, 27(4): 047203. **doi:** 10.1088/1674-1056/27/4/047203

Band engineering and precipitation enhance thermoelectric performance of SnTe with Zn-doping

Zhiyu Chen(陈志禹), Ruifeng Wang(王瑞峰), Guoyu Wang(王国玉), Xiaoyuan Zhou(周小元), Zhengshang Wang(王正上), Cong Yin(尹聪), Qing Hu(胡庆), Binqiang Zhou(周斌强), Jun Tang(唐军), Ran Ang(昂然)
Chin. Phys. B . 2018, 27(4): 047202. **doi:** 10.1088/1674-1056/27/4/047202

Biaxial strain-induced enhancement in the thermoelectric performance of monolayer WSe_2

Wanhuizi Shen(沈婉慧子), Daifeng Zou(邹代峰), Guozheng Nie(聂国政), Ying Xu(许英)
Chin. Phys. B . 2017, 26(11): 117202. **doi:** 10.1088/1674-1056/26/11/117202

Charge and spin-dependent thermal efficiency of polythiophene molecular junction in presence of dephasing

Z. Golsanamlou, M. Bagheri Tagani, H. Rahimpour Soleimani
Chin. Phys. B . 2015, 24(10): 108402. **doi:** 10.1088/1674-1056/24/10/108402

TOPICAL REVIEW — Recent advances in thermoelectric materials and devices

Fundamental and progress of Bi_2Te_3-based thermoelectric materials*

Min Hong(洪敏)[1,2], Zhi-Gang Chen(陈志刚)[1,2,†], and Jin Zou(邹进)[2,3,‡]

[1] Centre of Future Materials, the University of Southern Queensland (USQ), Springfield, Queensland 4300, Australia
[2] Materials Engineering, University of Queensland, Brisbane, Queensland 4072, Australia
[3] Centre for Microscopy and Microanalysis, University of Queensland, Brisbane, Queensland 4072, Australia

(Received 23 January 2018; revised manuscript received 2 March 2018; published online 29 March 2018)

Thermoelectric materials, enabling the directing conversion between heat and electricity, are one of the promising candidates for overcoming environmental pollution and the upcoming energy shortage caused by the over-consumption of fossil fuels. Bi_2Te_3-based alloys are the classical thermoelectric materials working near room temperature. Due to the intensive theoretical investigations and experimental demonstrations, significant progress has been achieved to enhance the thermoelectric performance of Bi_2Te_3-based thermoelectric materials. In this review, we first explored the fundamentals of thermoelectric effect and derived the equations for thermoelectric properties. On this basis, we studied the effect of material parameters on thermoelectric properties. Then, we analyzed the features of Bi_2Te_3-based thermoelectric materials, including the lattice defects, anisotropic behavior and the strong bipolar conduction at relatively high temperature. Then we accordingly summarized the strategies for enhancing the thermoelectric performance, including point defect engineering, texture alignment, and band gap enlargement. Moreover, we highlighted the progress in decreasing thermal conductivity using nanostructures fabricated by solution grown method, ball milling, and melt spinning. Lastly, we employed modeling analysis to uncover the principles of anisotropy behavior and the achieved enhancement in Bi_2Te_3, which will enlighten the enhancement of thermoelectric performance in broader materials

Keywords: thermoelectric, Bi_2Te_3-based alloys, electron transports, phonon scatterings

PACS: 84.60.Rb, 74.25.fc, 72.10.–d, 61.72.Nn **DOI:** 10.1088/1674-1056/27/4/048403

1. Introduction

The rising demand for energy supply, the elimination of greenhouse gas due to carbon-based energy sources, and the enhancement in the energy consumption efficiency have sparked significant research into alternative energy sources and energy harvesting technologies. One of the promising candidates is thermoelectricity, in which heat is transferred directly into electricity.[1–3] Because of the distinct advantages of thermoelectric devices: no moving parts, long steady-state operation period, zero emission, precise temperature control and capable of function in extreme environment,[4–6] the prospect of thermoelectric applications is promising, especially for power generation and refrigeration. For the power generation mode, energy is captured from waste, environmental, or mechanical sources, and converted into an exploitable form — electricity by thermoelectric devices.[7–10] Thermoelectric materials are also able to generate power by using solar energy to create a temperature difference across thermoelectric materials.[11,12] Nuclear reactors and radioisotope thermoelectric generators can be used as spacecraft propulsion and for power supply.[13–16] For the refrigeration mode, micro thermoelectric cooling modules can be installed in the integrated circuit to tackle the heat-dissipation problem, and flexible thermoelectric materials can be equipped in the uniform of people working in the extreme environment to serve as the wearable climate control system.[17]

The wide application of thermoelectric materials requires high energy conversion efficiency and the enhancement involves the simultaneous management of several parameters. First, Seebeck coefficient (S), the generated voltage over the applied temperature, is defined. Since thermoelectric materials involve charge carrier transport and heat flow, electrical conductivity (σ) and thermal conductivity (κ) should be taken into account. To ensure a high output power, both S and σ should be as large as possible. To maintain the temperature difference across the material, a low κ is preferred. Accordingly, the dimensionless figure-of-merit, zT has been defined to quantify the thermoelectric performance at a given temperature (T), namely $zT = S^2\sigma T\kappa$.[1,18,19] The criteria of good thermoelectric materials are high power-factor ($S^2\sigma$ and low κ. $S^2\sigma$ can be enhanced by resonant state doping,[1,20,21] minority carrier blocking,[22] band convergence,[23–27] reversible phase transition,[28–30] and quantum confinement;[31,32] and κ can be reduced by nanostructuring,[33–39] hierarchical architecturing,[40–42] producing dislocations,[43–45] introducing stacking faults,[46,47] and incorporating nanoprecipitates into the matrix.[48–53]

Owing to the intensive theoretical studies and experimen-

*Project supported by the Australian Research Council. Zhi-Gang Chen thanks the USQ start-up grant and strategic research grant.
†Corresponding author. E-mail: zhigang.chen@usq.edu.au
‡Corresponding author. E-mail: j.zou@uq.edu.au
© 2018 Chinese Physical Society and IOP Publishing Ltd

tal demonstrations over the past decades, zT has been improved dramatically. Figures 1(a) and 1(b) plot the achieved state-of-the-art zT values for both n-type and p-type materials working over a wide temperature range. Bi_2Te_3, PbTe, and GeSi are the classical thermoelectric materials working near room-, mid-, and high-temperature, respectively.[5,54] Through band alignment, Na-doped $PbTe_{1-x}Se_x$ exhibited zT up to 1.8.[23] In addition, nanostructuring successfully improved zT for GeSe to over 1.[55] Moreover, SnTe, as an environmentally friendly lead-free thermoelectric candidate, exhibited zT over 1.2 through producing band convergence and introducing nanoprecipitates.[56–61] The lead-free SnSe with earth-abundant elements has attracted wide attention due to the reported record-high zT of 2.6 along the b axis of the single crystal.[28] Later on, Na-doping was employed to significantly enhance the mid-temperature zT for SnSe single crystal.[62–66]

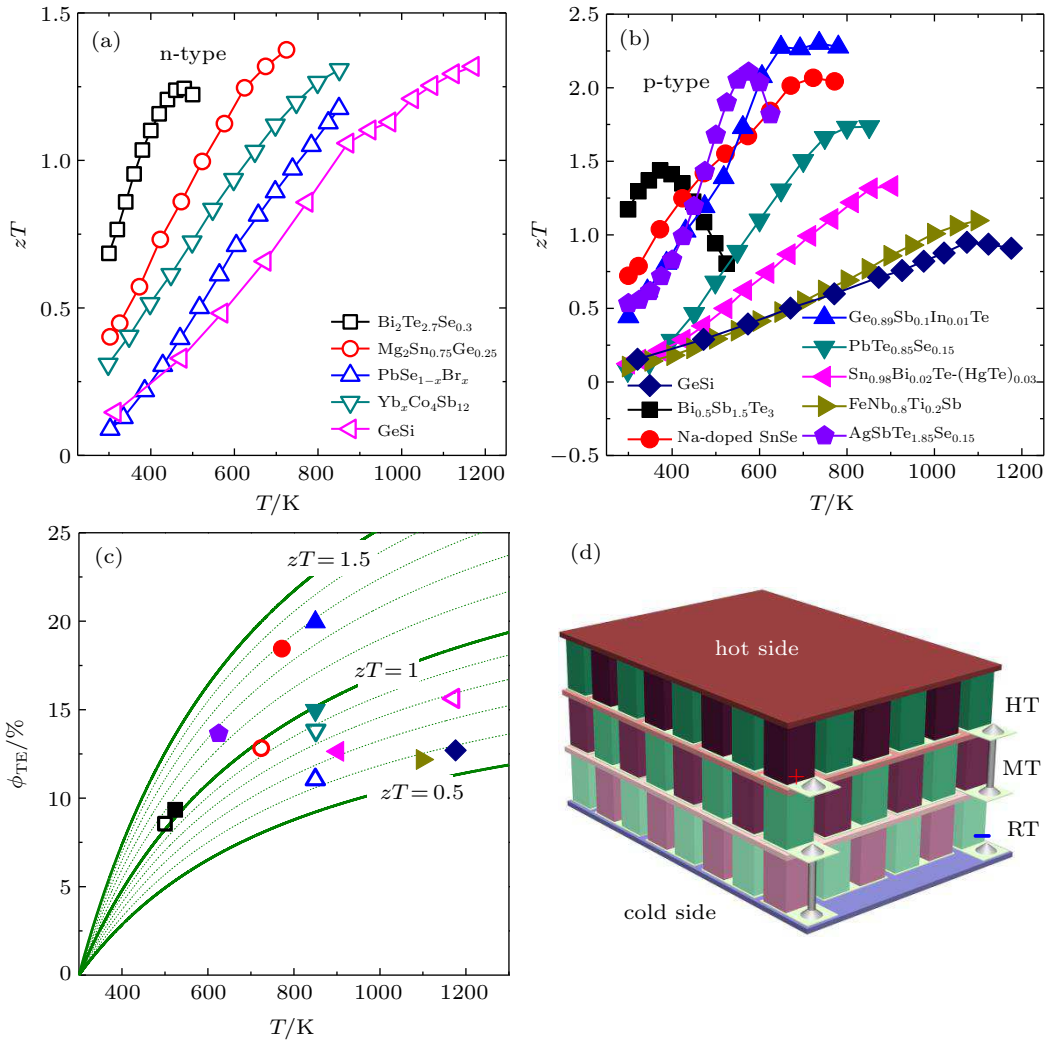


Fig. 1. (color online) The state-of-the-art zT values for n-type (a) $Bi_2Te_{2.7}Se_{0.3}$,[37] $Mg_2Sn_{0.75}Ge_{0.25}$,[25] $PbSe_{1-x}Br_x$,[67] $Yb_xCo_4Sb_{12}$,[68] and GeSi;[69] p-type (b) $Ge_{0.89}Sb_{0.1}In_{0.01}$,[47] $Bi_{0.5}Sb_{1.5}Te_3$,[70] $TePbTe_{0.85}Se_{0.15}$,[23] $Sn_{0.98}Bi_{0.02}Te$-$(HgTe)_{0.03}$,[60] $FeNb_{0.8}Ti_{0.2}Sb$,[71] $AgSbTe_{1.85}Se_{0.15}$,[46] and GeSi.[55] (c) Corresponding thermoelectric efficiency calculated using zT_{avg} values of these summarized materials. (d) The schematic diagram of a multi-layer thermoelectric device assembled from materials working at high (HT), mid (MT), and room (RT) temperatures along the thermal gradient from the hot side to the cold side.

The efficiency (ϕ_{TE}) of a thermoelectric device as a function of zT is calculated by[72,73]

$$\phi_{TE} = \frac{W}{Q_H} = \phi_C \left(\frac{\sqrt{1+zT}-1}{\sqrt{1+zT}+T_C/T_H} \right), \quad (1)$$

and ϕ_C is the Carnot efficiency, given by

$$\phi_C = \frac{T_H - T_C}{T_H}. \quad (2)$$

In the above equations, Q_H is the net heat flow rate, W is the generated electric power, T_C is the cold side temperature, and T_H is the hot side temperature, respectively.

According to Eq. (1), the dependence of thermoelectric efficiency on average zT (zT_{avg}) for single-leg state-of-the-art thermoelectric materials is plotted in Fig. 1(c), in which the cold side temperature is set as 300 K, and the hot side temperature is the corresponding temperature for peak zT. The efficiency of thermoelectric materials for room-temperature power generation is lower than 10%, for mid-temperature applications, the peak efficiency could be ~ 25%, and for high-

temperature applications, the efficiency is 22%.

To allow a maximum energy harvesting efficiency from a heat source, a thermoelectric device can be assembled by triple layers of p–n-junction arrays in a tandem mode, as shown in Fig. 1(d). The first layer is high-temperature thermoelectric materials, while the second and third layers are respectively built from mid- and low-temperature candidates as regenerative cycles. So far, Bi_2Te_3 families are still the most promising room-temperature thermoelectric candidates. It is necessary to dedicate significant research into this classical thermoelectric category.

In this review, we provide an overview of the development of Bi_2Te_3-based thermoelectric materials, including the fundamentals on thermoelectric effects, current research progress, and new trends in Bi_2Te_3-based thermoelectric materials. Firstly, we study the fundamentals of thermoelectric effects and find that thermoelectric effects are substantially the re-distribution of electrons disturbed by temperature difference or extra potential and the attendant energy exchange between the free charge carriers and environment. Also, we derived the model of electronic transport coefficients from the Boltzmann equation (BTE). On this basis, we performed simulations of the effect of materials' parameters on electronic transport coefficient. Secondly, we summarized the features of Bi_2Te_3-based thermoelectric materials and the correspondingly developed strategies for enhancing their thermoelectric performance. Finally, we quantitatively analyzed the reported data for Bi_2Te_3-based thermoelectric materials, which is believed to provide innovative directions for developing high-performance thermoelectric candidates in broader materials.

2. Thermoelectric effect

Thermoelectric effect includes Seebeck effect and Peltier effect.[74] Seebeck effect originates from the charge current flow driven by the temperature difference. Reversibly, the charge current flow driven by extra applied voltage can generate temperature difference across the material, which is Peltier effect.[75,76] In this regards, thermoelectric effect involves how temperature difference or extra voltage disturb the distribution of free charge carriers and the attendant energy exchange.[77]

At equilibrium, the distribution of free charge carriers, for instance, electrons, follows the Fermi–Dirac function, i.e.

$$f_0 = \frac{1}{\exp[(E-u)/k_{\mathrm{B}}T]+1}, \tag{3}$$

in which E is the energy level, u is the chemical potential, k_{B} is the Boltzmann constant, and T is temperature. Generally, u equals Fermi level (E_{f}).[78,79] If $E \gg u$, $f_0 = 0$, and if $E \ll u$, $f_0 = 1$. At 0 K, the transition of f_0 from 0 to 1 exactly occurs at u, while at non-zero K the transition of f_0 from 0 to 1 occurs over an energy window of a few $k_{\mathrm{B}}T$.[78] At a given E, f_0 is determined by both T and u. Therefore, the temperature and external potential (i.e., voltage) can change f_0 and consequently result in the re-distribution of charge carriers, ultimately leading to the charge current flow. In this context, we present a detailed discussion on the principle of thermoelectric effects.

Figure 2(a) shows a single-leg thermoelectric device consisting of a channel (thermoelectric material) with two contacts. T_i, u_i, and f_0^i are temperatures, chemical potentials, and Fermi–Dirac functions for the two contacts ($i = 1$ and 2 representing the left and right contacts), respectively. The competition between f_0^1 and f_0^2 , i.e., $f_0^1 - f_0^2$, accounts for the charge current flow through the channel. Without temperature or potential disturbances, (i.e., $T_1 = T_2$ and $u_1 = u_2$), $f_0^1 - f_0^2 = 0$. When $T_1 > T_2$ but $u_1 = u_2$ (namely, applying a temperature difference) the transition of f_1 from 0 to 1 occurs over a wider energy window than f_2 does, which means at an energy higher than the chemical potential, $f_0^1 - f_0^2 > 0$, otherwise $f_0^1 - f_0^2 < 0$. Electrons with energy higher than the chemical potential flow from the left contact to the right contact, while electrons with lower energy flow from the right contact to the left contact. Despite f_0, the other factor affecting the number of electrons at a certain energy is the density of states (DOS, $g(E)$), which describes the possible states of electrons at the energy level of E.[80] In Fig. 2(a), the plotted $g(E)$ corresponds to n-type semiconductors and increases with increasing energy level, indicative of more electron states at the higher energy level. Consequently, the net electron current flows from hot side to cold side, resulting in the hot side to be positive and the cold side to be negative. Thus, u_1 becomes lower than u_2, and the difference between u_1 and u_2 increases when more and more electrons accumulate on the code side. Note that negative electrode has a higher potential for electrons. Figure 2(b) describes the updated $f_0^1 - f_0^2$ at equilibrium, and there is no net electron flow.

For the Peltier effect, the temperature difference is generated by charge current flow, which is driven by the external voltage. Figure 2(c) is the schematic illustrating the Peltier effect, in which an external voltage is applied to the two contacts, for example, left contact being negative and right contact being positive, i.e., $u_1 > u_2$ for electrons, leading to the electron current flows from left to right. For simplicity, the channel is regarded as an elastic resistor, in which the electrons current does not lose energy and energy exchange only occurs at the two contacts. For the right contact, the arrival electrons with a higher energy of E_{e} should release energy by an amount of $Q_{\mathrm{rel}} = E_{\mathrm{e}} - u_2$ per each electron. On the other hand, the provided electrons from the left contact should absorb energy to climb to the higher energy level of E_{e} and the required energy value is $Q_{\mathrm{abs}} = E_{\mathrm{e}} - u_1$ per each electron. Accordingly, the left contact is cooled down, resulting in $T_1 < T_2$. Therefore, $f_0^1 - f_0^2$ varies, as shown in Fig. 2(d). Finally, there is no net

electron flow at the equilibrium. Note that within the framework of elastic resistor, $Q_{\rm rel} - Q_{\rm abs} = u_1 - u_2$, which is the potential difference provided by the external power; however, the practical thermoelectric materials are inelastic resistor because of the inelastic electron-electron and electron-nucleus collisions, which means electron current loses energy inside the thermoelectric materials in the form of heat, resulting in $Q_{\rm rel} - Q_{\rm abs} < u_1 - u_2$, namely the input power is higher than the generated heat energy difference.

Based on above discussion, charge current flow results from the disturbance of Fermi–Dirac function, which can be motivated by the temperature difference and the external potential. Seebeck effect is the Fermi–Dirac function disturbed by the temperature difference. Working under the power generation mode, the cold side corresponds to the negative pole of n-type, while the hot side corresponds to the negative pole of p-type. Peltier effect is the energy exchange between the free electrons and the contacts when Fermi–Dirac function is disturbed by an external potential. Working under the refrigeration mode, the negative pole is cooled down for n-type, while positive pole is cooled down for p-type.

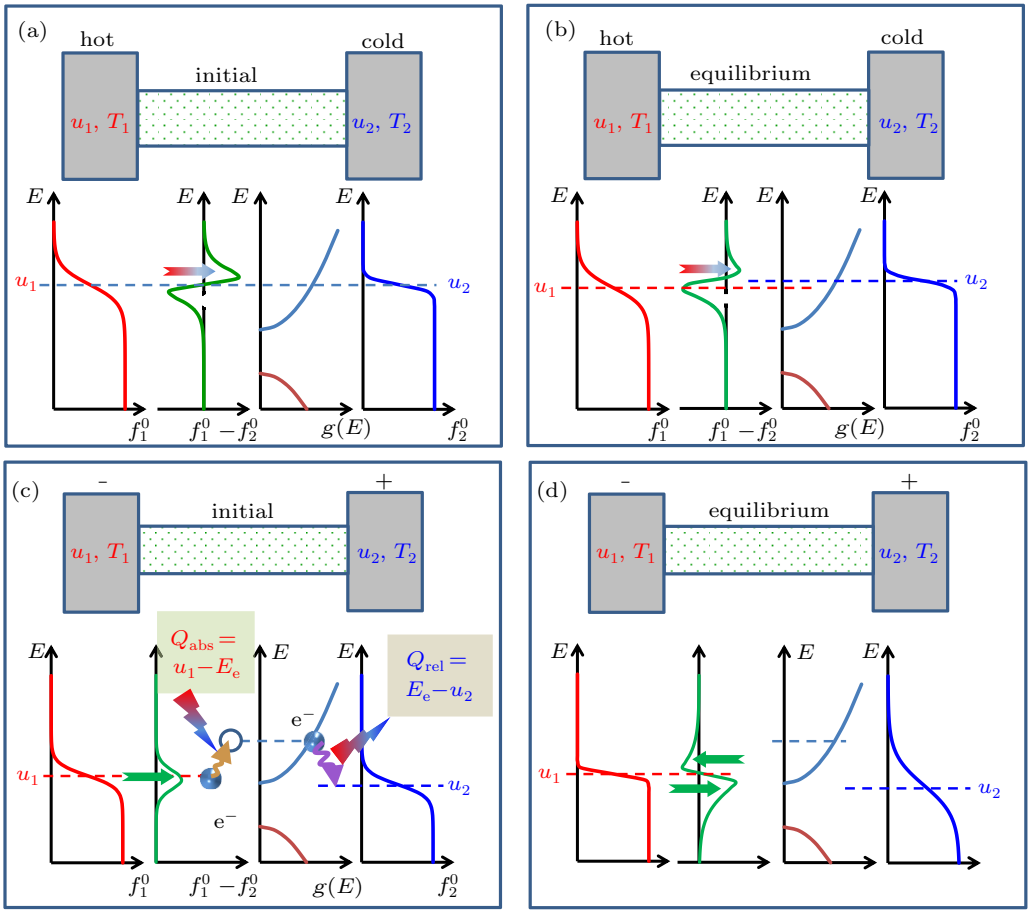


Fig. 2. (color online) Seebeck effect with charge current driven by the temperature difference for n-type thermoelectric materials: (a) the initial stage and (b) equilibrium. (c) Peltier effect with charge current driven by the voltage for n-type thermoelectric materials: (c) the initial stage and (d) equilibrium.

3. Equations of electronic transport coefficients from Boltzmann equation (BTE)

3.1. Definition of electronic transport coefficients

Thermoelectric effect involves charge current flow and heats current flow. Noteworthy, the heat current specifically refers to the thermal energy transported by charge current. By definition, charge current density (J), and heat current density (Q) are respectively expressed by[32]

$$J \equiv nev = e\int_{-\infty}^{+\infty} v(E)g(E)\left[f(E) - f_0(E)\right]\mathrm{d}E, \tag{4}$$

$$Q \equiv n(E-u)v = \int_{-\infty}^{+\infty} v(E)(E-u)g(E)\left[f(E) - f_0(E)\right]\mathrm{d}E, \tag{5}$$

in which, n is the carrier concentration, e is the free electron charge, and v is the carrier velocity.

On this basis, σ, S, and the electrical thermal conductivity ($\kappa_{\rm e}$) can be defined as[80]

$$\sigma \equiv \left.\frac{J}{\varepsilon}\right|_{\nabla_x T=0}, \tag{6}$$

$$S \equiv \left.\frac{\varepsilon}{\nabla_x T}\right|_{J=0}, \tag{7}$$

$$\kappa_{\rm e} \equiv -\left.\frac{Q}{\nabla_x T}\right|_{J=0} \tag{8}$$

with ε denoting the intensity of the electrical field. Equation (6) is based on the Ohm's law without a temperature gradient. Equations (7) and (8) are the thermoelectric generator working under an open circuit. The negative sign in Eq. (8) means that thermal energy is lost.

3.2. Steady state solution to Boltzmann equation

From Eqs. (4)–(8), the derivations of S, σ, and κ_e are actually to determine $f(E)-f_0(E)$ in Eqs. (4) and (5), which is the steady-state solution to the Boltzmann equation (BTE).[81,82] BTE is

$$\left(\frac{\partial f}{\partial t}\right)_{\text{field}}+\left(\frac{\partial f}{\partial t}\right)_{\text{collision}}=0, \tag{9}$$

in which f, as functions of time (t), wave vectors ($\boldsymbol{k}$), and position vectors ($\boldsymbol{x}$), is the non-equilibrium distribution function of electrons. The first term of Eq. (9) represents how the external fields (including electrical and temperature fields in thermoelectric materials) affect f.[83] The second term of Eq. (9) represents the effect of collisions (or, scattering) that prevents electrons from infinitely accelerating under external forces. The reason for Eq. (9) $=0$ is that electrons do not move outside in an open circuit at any time.

Under the relaxation time approximation,[84] i.e.

$$\left(\frac{\partial f}{\partial t}\right)_{\text{collision}}=\frac{f-f_0}{\tau}, \tag{10}$$

in which τ is the relaxation time of electrons, and f_0 is electron distribution at equilibrium as described in Eq. (3).

The first term of BTE is

$$\left(\frac{\partial f}{\partial t}\right)_{\text{field}}=\frac{\partial f}{\partial t}+\frac{\partial f}{\partial \boldsymbol{x}}\frac{\partial \boldsymbol{x}}{\partial t}+\frac{\partial f}{\partial \boldsymbol{k}}\frac{\partial \boldsymbol{k}}{\partial t}. \tag{11}$$

Here, we want to derive the steady-state solution to the BTE, thus

$$\frac{\partial f}{\partial t}=0. \tag{12}$$

In addition, based on the momentum theory, we have

$$\hbar\partial \boldsymbol{k}=F\partial t, \tag{13}$$

namely

$$\frac{\partial \boldsymbol{k}}{\partial t}=\frac{F}{\hbar}, \tag{14}$$

in which, $\hbar$ is the reduced Planck constant, and F is a generalized form of force. In the case of an electric field, F equals $e\varepsilon$.[85]

Through substituting Eqs. (12) and (14) into Eq. (11), we have

$$\left(\frac{\partial f}{\partial t}\right)_{\text{field}}=\boldsymbol{v}\nabla_x f+\frac{F}{\hbar}\nabla_k f, \tag{15}$$

with the velocity vector (v),

$$\nabla_x f=\frac{\partial f}{\partial \boldsymbol{x}}=\frac{\partial f}{\partial E}\frac{\partial E}{\partial T}\frac{\partial T}{\partial \boldsymbol{x}}=\frac{\partial f}{\partial E}\left(\frac{E-u}{T}\right)\nabla_x T, \tag{16}$$

$$\nabla_k f=\frac{\partial f}{\partial \boldsymbol{k}}=\frac{\partial f}{\partial E}\frac{\partial E}{\partial \boldsymbol{k}}\xrightarrow{\partial E/\partial \boldsymbol{k}=\hbar k/m^*}\frac{\partial f}{\partial E}\frac{\hbar^2 k}{m^*}. \tag{17}$$

Thus, equation (15) becomes

$$\begin{aligned}\left(\frac{\partial f}{\partial t}\right)_{\text{field}} &= \boldsymbol{v}\frac{\partial f}{\partial E}\frac{E-u}{T}\nabla_x T+\frac{F}{\hbar}\frac{\partial f}{\partial E}\frac{\hbar^2 k}{m^*}\\ &= \frac{\partial f}{\partial E}\left(\boldsymbol{v}\frac{E-u}{T}\nabla_x T+\frac{F}{\hbar}\frac{\hbar^2 k}{m^*}\right)\\ &\xrightarrow{\boldsymbol{v}=\hbar k/m^*} \frac{\partial f}{\partial E}\left(\boldsymbol{v}\frac{E-u}{T}\nabla_x T+\boldsymbol{v}F\right)\\ &= \frac{\partial f}{\partial E}\boldsymbol{v}\left(\frac{E-u}{T}\nabla_x T+F\right).\end{aligned} \tag{18}$$

Based on Eqs. (9), (10), and (18), the steady state solution to the BTE is

$$\begin{aligned}f-f_0 &= -\boldsymbol{v}\tau\frac{\partial f}{\partial E}\left(\frac{E-u}{T}\nabla_x T+F\right)\\ &\xrightarrow{F=e\varepsilon,\,f\approx f_0} -\boldsymbol{v}\tau\frac{\partial f_0}{\partial E}\left(\frac{E-u}{T}\nabla_x T+e\varepsilon\right).\end{aligned} \tag{19}$$

3.3. Derivation of electronic transport coefficients

(i) Electrical conductivity

$$\begin{aligned}\sigma &\equiv \left.\frac{J}{\varepsilon}\right|_{\nabla_x T=0}=\frac{e}{\varepsilon}\int_{-\infty}^{+\infty}\boldsymbol{v}(E)g(E)\left[f(E)-f_0(E)\right]\mathrm{d}E\\ &= \frac{e}{\varepsilon}\int_{-\infty}^{+\infty}\boldsymbol{v}(E)g(E)\boldsymbol{v}\tau\left(-\frac{\partial f_0}{\partial E}\right)\left(\frac{E-u}{T}\nabla_x T+e\varepsilon\right)\mathrm{d}E\\ &= e^2\int_{-\infty}^{+\infty}\boldsymbol{v}^2(E)g(E)\tau\left(-\frac{\partial f_0}{\partial E}\right)\mathrm{d}E.\end{aligned} \tag{20}$$

(ii) Carrier concentration (n)

Carrier concentration (n) is derived from the definition, namely

$$n=\int_0^{\infty}g(E)f_0(E)\mathrm{d}E. \tag{21}$$

Then, drift mobility is

$$\mu=\frac{\sigma}{ne}. \tag{22}$$

Practically, Hall effect is employed to characterize the electronic transport. Hall carrier concentration and Hall carrier mobility are given by

$$n_{\text{H}}=\frac{n}{A}, \tag{23}$$

$$\mu_{\text{H}}=\mu A, \tag{24}$$

in which A is the Hall factor and can be expressed as

$$A=\frac{\dfrac{\displaystyle\int_0^{\infty}g(E)\tau^2(E)v^2(E)\left(-\dfrac{\partial f}{\partial E}\right)\mathrm{d}E}{\displaystyle\int_0^{\infty}g(E)v^2(E)\left(-\dfrac{\partial f}{\partial E}\right)\mathrm{d}E}}{\left(\dfrac{\displaystyle\int_0^{\infty}g(E)\tau(E)v^2(E)\left(-\dfrac{\partial f}{\partial E}\right)\mathrm{d}E}{\displaystyle\int_0^{\infty}g(E)v^2(E)\left(-\dfrac{\partial f}{\partial E}\right)\mathrm{d}E}\right)^2}. \tag{25}$$

(iii) Seebeck coefficient

The derivation of S is based on $J=0$. From Eqs. (4) and (19), we have

$$J = e\int_{-\infty}^{+\infty} v(E)g(E)\boldsymbol{v}\tau\left(-\frac{\partial f_0}{\partial E}\right)\left(\frac{E-u}{T}\nabla_x T + e\boldsymbol{\varepsilon}\right)\mathrm{d}E = 0. \tag{26}$$

Thus,

$$\boldsymbol{\varepsilon} = -\frac{\nabla_x T\int_{-\infty}^{+\infty} v(E)g(E)\boldsymbol{v}\tau\left(-\frac{\partial f_0}{\partial E}\right)\left(\frac{E-u}{T}\right)\mathrm{d}E}{e\int_{-\infty}^{+\infty} v(E)g(E)\boldsymbol{v}\tau\left(-\frac{\partial f_0}{\partial E}\right)\mathrm{d}E}. \tag{27}$$

So,

$$\begin{aligned} S &\equiv \left.\frac{\boldsymbol{\varepsilon}}{\nabla_x T}\right|_{J=0} \\ &= -\frac{\nabla_x T\int_{-\infty}^{+\infty} v(E)g(E)\boldsymbol{v}\tau\left(-\frac{\partial f_0}{\partial E}\right)\left(\frac{E-u}{T}\right)\mathrm{d}E}{\nabla_x Te\int_{-\infty}^{+\infty} v(E)g(E)\boldsymbol{v}\tau\left(-\frac{\partial f_0}{\partial E}\right)\mathrm{d}E} \\ &= -\frac{1}{eT}\left[\frac{\int_{-\infty}^{+\infty}\boldsymbol{v}^2(E)g(E)\tau E\left(-\frac{\partial f_0}{\partial E}\right)\mathrm{d}E}{\int_{-\infty}^{+\infty}\boldsymbol{v}^2(E)g(E)\tau\left(-\frac{\partial f_0}{\partial E}\right)\mathrm{d}E} - \mu\right]. \end{aligned} \tag{28}$$

(iv) Electrical thermal conductivity and Lorenz number (L)

Based on Eqs. (4) and (5), we have

$$\begin{aligned} Q &= \int_{-\infty}^{+\infty} v(E)\,(E-u)\,g(E)\,[f(E)-f_0(E)]\,\mathrm{d}E \\ &= \int_{-\infty}^{+\infty} v(E)Eg(E)\,[f(E)-f_0(E)]\,\mathrm{d}E \\ &\quad -u\int_{-\infty}^{+\infty} v(E)g(E)\,[f(E)-f_0(E)]\,\mathrm{d}E \\ &= \int_{-\infty}^{+\infty} v(E)Eg(E)\,[f(E)-f_0(E)]\,\mathrm{d}E \\ &\quad -\frac{u}{e}e\int_{-\infty}^{+\infty} v(E)g(E)\,[f(E)-f_0(E)]\,\mathrm{d}E \\ &= \int_{-\infty}^{+\infty} v(E)Eg(E)\,[f(E)-f_0(E)]\,\mathrm{d}E - \frac{u}{e}J. \end{aligned} \tag{29}$$

Since in the derivation of $\kappa_e J=0$,

$$Q = \int_{-\infty}^{+\infty} v(E)Eg(E)\,[f(E)-f_0(E)]\,\mathrm{d}E. \tag{30}$$

Therefore,

$$\begin{aligned} \kappa_e &\equiv \left.-\frac{Q}{\nabla_x T}\right|_{J=0} \\ &= -\frac{1}{\nabla_x T}\int_{-\infty}^{+\infty} v(E)Eg(E)\,[f(E)-f_0(E)]\,\mathrm{d}E \\ &= -\frac{1}{T}\int_{-\infty}^{+\infty}\boldsymbol{v}^2(E)Eg(E)\tau\left(-\frac{\partial f_0}{\partial E}\right)(E-u)\,\mathrm{d}E \\ &\quad -\frac{e\boldsymbol{\varepsilon}}{\nabla_x T}\int_{-\infty}^{+\infty}\boldsymbol{v}^2(E)Eg(E)\tau\left(-\frac{\partial f_0}{\partial E}\right)\mathrm{d}E. \end{aligned} \tag{31}$$

Substituting Eq. (27) into above equation, we have

$$\begin{aligned} \kappa_e &= -\frac{1}{T}\int_{-\infty}^{+\infty}\boldsymbol{v}^2(E)Eg(E)\tau\left(-\frac{\partial f_0}{\partial E}\right)(E-u)\,\mathrm{d}E, \\ &\quad +\frac{\int_{-\infty}^{+\infty}\boldsymbol{v}^2(E)g(E)\tau\left(-\frac{\partial f_0}{\partial E}\right)\left(\frac{E-u}{T}\right)\mathrm{d}E}{\int_{-\infty}^{+\infty}\boldsymbol{v}^2(E)g(E)\tau\left(-\frac{\partial f_0}{\partial E}\right)\mathrm{d}E} \\ &\quad \times\int_{-\infty}^{+\infty}\boldsymbol{v}^2(E)Eg(E)\tau\left(-\frac{\partial f_0}{\partial E}\right)\mathrm{d}E, \\ &= -\frac{1}{T}\int_{-\infty}^{+\infty}\boldsymbol{v}^2(E)E^2g(E)\tau\left(-\frac{\partial f_0}{\partial E}\right)\mathrm{d}E \\ &\quad +\frac{\left(\int_{-\infty}^{+\infty}\boldsymbol{v}^2(E)g(E)\tau E\left(-\frac{\partial f_0}{\partial E}\right)\mathrm{d}E\right)^2}{T\int_{-\infty}^{+\infty}\boldsymbol{v}^2(E)g(E)\tau\left(-\frac{\partial f_0}{\partial E}\right)\mathrm{d}E}. \end{aligned} \tag{32}$$

According to Wiedemann–Franz law,[86] Lorenz number is

$$L \equiv \frac{\kappa_e}{\sigma T}. \tag{33}$$

Substituting Eqs. (20) and (32) into Eq. (33), we have

$$\begin{aligned} L &= -\frac{1}{T^2e^2}\left(\frac{\int_{-\infty}^{+\infty}\boldsymbol{v}^2(E)E^2g(E)\tau\left(-\frac{\partial f_0}{\partial E}\right)\mathrm{d}E}{\int_{-\infty}^{+\infty}\boldsymbol{v}^2(E)g(E)\tau\left(-\frac{\partial f_0}{\partial E}\right)\mathrm{d}E}\right. \\ &\quad \left.-\left(\frac{\int_{-\infty}^{+\infty}\boldsymbol{v}^2(E)g(E)\tau E\left(-\frac{\partial f_0}{\partial E}\right)\mathrm{d}E}{\int_{-\infty}^{+\infty}\boldsymbol{v}^2(E)g(E)\tau\left(-\frac{\partial f_0}{\partial E}\right)\mathrm{d}E}\right)^2\right). \end{aligned} \tag{34}$$

So far, we derived σ, S, κ_e, and L, expressed by Eqs. (20), (28), (32), and (34), respectively.

3.4. Kane band model

In the non-parabolic band with energy dispersion described by Kane relation, the DOS can be expressed as[87]

$$g(E) = \frac{\sqrt{2}N_v m_b^{*3/2}}{\pi^2\hbar^3}E^{1/2}\left(1+\frac{E}{E_g}\right)^{1/2}\left(1+2\frac{E}{E_g}\right). \tag{35}$$

Under the assumption of acoustic phonons dominating carrier scattering, carrier relaxation time is[88,89]

$$\begin{aligned} \tau(\varepsilon) &= \frac{2\pi\hbar^4C_l}{(k_BT)^2(2m_b^*)^{3/2}E_{def}^2}E^{-1/2}\left(1+\frac{E}{E_g}\right)^{-1/2}\left(1+2\frac{E}{E_g}\right)^{-1} \\ &\quad \times\left[1-\frac{8\frac{E}{E_g}\left(1+\frac{E}{E_g}\right)}{3\left(1+2\frac{E}{E_g}\right)^2}\right]^{-1}. \end{aligned} \tag{36}$$

By substituting $g(E)$ and $\tau(E)$ into the derived thermoelectric properties, we can have the single Kane band model[90]

$$S = \frac{k_B}{e}\left[\frac{F_{1,-2}^1(\eta,\beta)}{F_{1,-2}^0(\eta,\beta)} - \eta\right], \tag{37}$$

$$\sigma = \frac{2e^2 N_v \hbar C_l}{\pi m_I^* E_{def}^2} F_{1,2}^0(\eta,\beta), \tag{38}$$

$$L = \left(\frac{k_B}{e}\right)^2 \left[\frac{F_{1,-2}^2(\eta,\beta)}{F_{1,-2}^0(\eta,\beta)} - \left(\frac{F_{1,-2}^1(\eta,\beta)}{F_{1,-2}^0(\eta,\beta)}\right)^2\right]. \tag{39}$$

Hall carrier concentration

$$n_H = \frac{N_v \left(2m_b^* k_B T\right)^{3/2}}{3\pi^2\hbar^3} \frac{F_{3/2,0}^0(\eta,\beta)}{A}. \tag{40}$$

Hall carrier mobility

$$\mu_H = A \frac{2\pi\hbar^4 e C_l}{m_I^* \left(2m_b^* k_B T\right)^{3/2} E_{def}^2} \frac{3F_{1,-2}^0(\eta,\beta)}{F_{3/2,0}^0(\eta,\beta)}. \tag{41}$$

Hall factor

$$A = \frac{3K(K+2)}{(2K+1)^2} \frac{F_{1/2,-4}^0 F_{3/2,0}^0}{\left(F_{1,-2}^0\right)^2}. \tag{42}$$

Generalized Fermi integration

$$F_{m,k}^n(\eta,\beta) = \int_0^\infty \left[-\frac{\partial f(\eta)}{\partial\varepsilon}\right] \varepsilon^n \left(\varepsilon + \beta\varepsilon^2\right)^m \times \left[(1+2\beta\varepsilon)^2 + 2\right]^{k/2} \mathrm{d}\varepsilon, \tag{43}$$

where η is the reduced Fermi level (for electrons, $\eta_e = (E_f - E_c)/(k_B T)$ with E_c denoting the conduction band edge; for holes,

$$\eta_h = \frac{E_v - E_f}{k_B T} = \frac{E_c - E_g - E_f}{k_B T} = -1/\beta - \eta_e$$

with E_v denoting the valance band edge), β is reciprocal of reduced band gap (i.e., $\beta = k_B T/E_g$), k_B is the Boltzmann constant, $\hbar$ is the reduced Planck constant, N_v is the band degeneracy, K is the ratio of longitudinal ($m_\parallel^*$) and transverse ($m_\perp^*$) effective mass, C_l is the combination of elastic constants, m_b^* is the band effective mass, m_I^* is the inertial effective mass, e is free electron charge, m_0 is the free electron mass, and E_{def} is the deformation potential, respectively. The relations of m_b^*, m_I^*, and density of state (DOS) effective mass (m_d^*) are expressed as

$$m_b^* = N^{-2/3} m_d^* \tag{44}$$

and

$$m_I^* = N^{-2/3} m_d^* \frac{3K^{2/3}}{2K+1}. \tag{45}$$

In some cases with notable bipolar conduction, we should consider both valance band and conduction band.[91,92]

Total Seebeck coefficient

$$S_{tot} = \frac{S_{CB}\sigma_{CB} + S_{VB}\sigma_{VB}}{\sigma_{CB} + \sigma_{VB}}. \tag{46}$$

Total electrical conductivity

$$\sigma_{tot} = \sigma_{CB} + \sigma_{VB}. \tag{47}$$

Total Hall coefficient

$$R_{Htot} = \frac{R_{HCB}\sigma_{CB}^2 + R_{HVB}\sigma_{VB}^2}{(\sigma_{CB} + \sigma_{VB})^2}. \tag{48}$$

Bipolar thermal conductivity

$$\kappa_{bi} = \frac{\sigma_{CB}\sigma_{VB}}{\sigma_{CB} + \sigma_{VB}} (S_{CB} - S_{VB})^2 T. \tag{49}$$

Total value of L

$$L_{tot} = \frac{L_{CB}\sigma_{CB} + L_{VB}\sigma_{VB}}{\sigma_{CB} + \sigma_{VB}}. \tag{50}$$

In the above equations, the components contributed by conduction band (CB) and valence band (VB) are presented by the corresponding subscripts. It should be mentioned that S and R_H are positive for p-type but negative for n-type in those equations.

4. Modeling studies of the parameters affecting thermoelectric properties of Bi_2Te_3

Based on above equations, we calculated the electronic transport coefficients as a function of η for Bi_2Te_3. Figure 3(a) shows the calculated σ as a function of η at 300 K with the inset illustrating the variation of η in the band structure. Note that we used $E_g = 0.15$ eV, and set the VB maximum as 0, which means the CB minimum is at 0.15 eV in energy. Therefore, at 300 K, $\eta = -5.8$ corresponding to the CB minimum. Moreover, considering the identical band effective mass for CB and VB, the middle point of band gap region is at $\eta = \sim -3$. As a consequence, σ for n-type (left side of -3) and p-type (right side of -3) is identical, and the total σ (blue curve) is generally superimposed with the CB component (red curve) for n-type and VB component (green curve) for p-type, respectively. Furthermore, in the whole studied η range, σ increases with enlarging $|\eta|$ for either n-type or p-type. The observed characteristics of symmetry (i.e., the calculated curve as a function of η is symmetrical relative to the middle of band gap region) and superimposition (i.e., the total value is respectively superimposed with the CB/VB component for n/p-type situation) also appear in the other calculated thermoelectric properties.

Figure 3(b) shows the calculated S as a function of η at 300 K. The characteristics of symmetry and superimposition are also observed in $|S|$. When $-5.8 < \eta < 0$, the total S is different from each component contributed by either CB or VB, which reveals n/p-type transition, i.e., the bipolar conduction. The peak value of $|S|$ depends on the onset of bipolar conduction, and $|S|$ decreases with increasing $|\eta|$ for either n-type or p-type. Based on the calculated S and σ, the plots of $S^2\sigma$ as a function of η at 300 K were obtained, as shown in Fig. 3(c). Likewise, $S^2\sigma$ also shows symmetrical and superimposing characteristics. Because of the bipolar conduction, the positions of total $S^2\sigma$ peaks are slightly different from the CB/VB components. If the η corresponding to the peak of

$S^2\sigma$ is defined as the optimized η (η^{opt}), η^{opt} for is 0.25 and −6.05 for p-type and n-type, respectively.

Figure 3(d) shows the plots of L as a function of η at 300 K. We can observe the superimposing and symmetrical features, and L increases with increasing $|\eta|$. Based on the calculated σ and L, we calculated κ_e, shown in Fig. 3(e), from which κ_e increases with increasing $|\eta|$. Figure 3(f) shows the calculated κ_{bi}. As can be seen, κ_{bi} is prominent in the band gap region and reaches the maximum value in the middle of band gap region. Moreover, κ_{bi} decreases with increasing $|\eta|$, because large $|\eta|$ makes it more difficult to activate minor carriers.

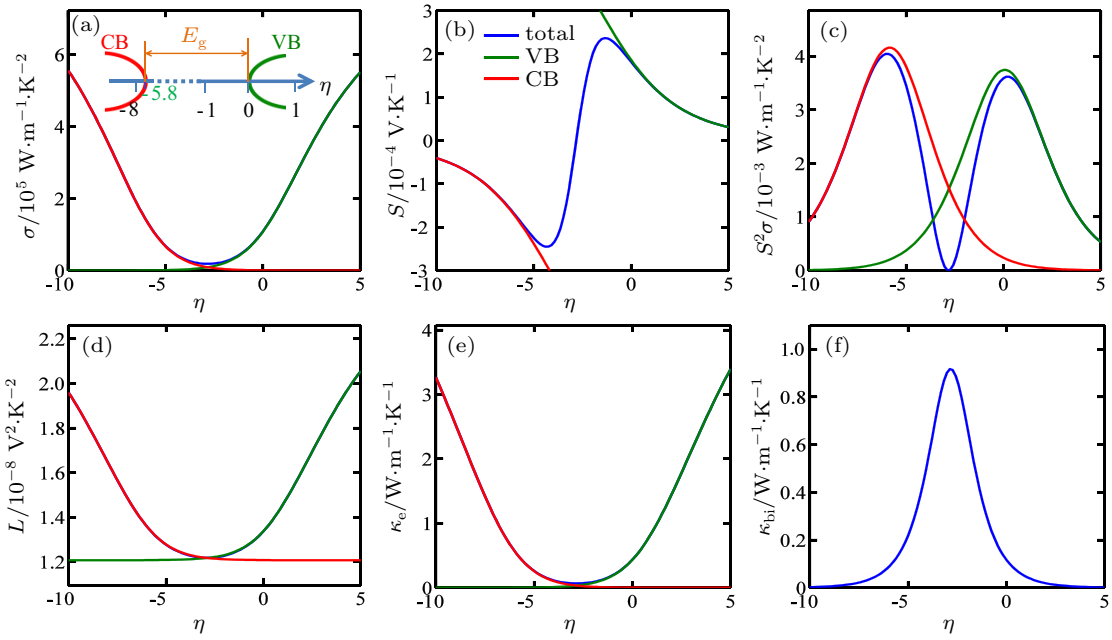


Fig. 3. (color online) Calculated (a) S, (b) σ, (c) $S^2\sigma$, (d) L, (e) κ_e, and (f) κ_e as a function of η at 300 K with the blue curve representing the total values, the purple curve representing the CB component, green curve representing the VB component.

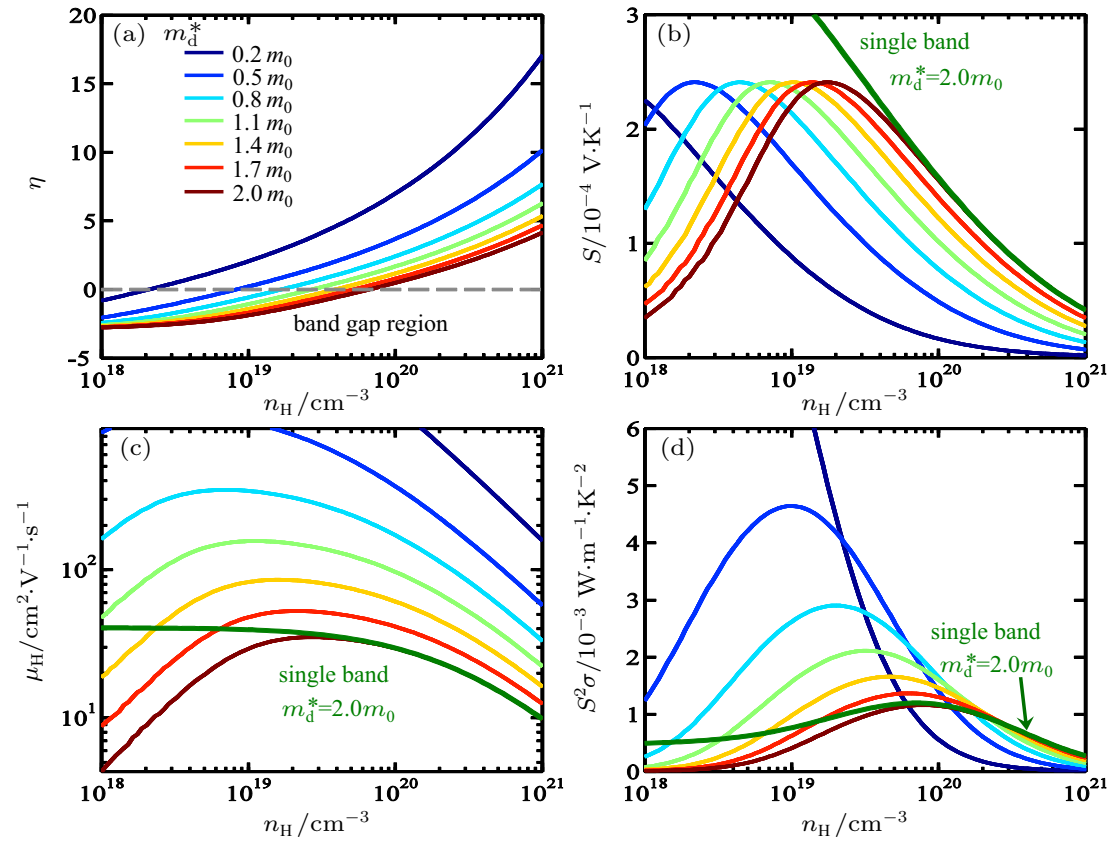


Fig. 4. (color online) (a) Determined η with n_H ranging from 10^{18} cm^{-3} to 10^{21} cm^{-3} for evenly selected seven m_d^* values from $0.2m_0$ to $2m_0$. Correspondingly calculated (b) S, (c) μ_H, and (d) $S^2\sigma$ as a function of n_H for different m_d^* values. The bold green lines in panels (b) and (c) are calculated using single band model with $m_d^* = 2m_0$ for S and μ_H, respectively.

Based on above discussions, S and σ are inversely related to η, resulting in a peak for $S^2\sigma$. Bipolar conduction has further limited the maximum values of S for n/p-type materials, therefore, the possible maximum values for $S^2\sigma$ is even smaller by considering both CB and VB. In addition to the electrical energy, the charge carriers can also transport thermal energy in the form of κ_e and κ_{bi}, which are anticipated to reduce the ultimate zT.

Based on the Kane band model, we can see S is only related to η and $\beta(=k_BT/E_g)$. Apart from η and β, n_H, and μ_H are determined by m_d^*, m_I^*, and E_{def}. Therefore, σ, κ_e, and κ_{bi} are also related to these parameters. Through band engineering, we can tune these parameters to tailor the electronic transport. Here, we quantitatively predict the effects of m_d^*, E_{def}, and E_g on the electronic transport properties. Note that from the Kane model equations, all thermoelectric properties are direct as a function of η. Here, we want to examine the variations of these thermoelectric properties with n_H.

Figure 4(a) shows the determined η with n_H ranging from 10^{18} cm^{-3} to 10^{21} cm^{-3} for evenly selected seven m_d^* values from $0.2m_0$ to $2m_0$. With increasing n_H, η monotonically increases, and with increasing m_d^*, η decreases for a given n_H, which results in the E_f corresponding to high n_H still resides in the band gap region for large m_d^*. Thus, larger m_d^* would unfavorably lead to a strong bipolar conduction. Based on the determined η, figures 4(b)–4(d) show the effects of m_d^* on n_H-dependent S, μ_H, and $S^2\sigma$, respectively. With increasing n_H, both S and μ_H increase and then decrease. Moreover, we observed that the calculated variation of S and μ_H at low n_H is different from the monotonic decreasing trends in both S and μ_H with increasing n_H calculated by the single band model (refer to the bold green lines in Figs. 4(b) and 4(c)). The observed difference suggests that, at low n_H region (band gap region), both S and μ_H calculated by the two bands model are lower than those from single band model, and the reason is ascribed to the bipolar conduction. Moreover, with increasing m_d^*, S increases, while μ_H decreases, and μ_H is more sensitive to the variation of m_d^*. As a consequence, $S^2\sigma$ decreases with increasing m_d^*, as shown in Fig. 4(d). In addition, optimal n_H (n_H^{opt}) corresponding to the peak $S^2\sigma$ shifts to a higher value with increasing m_d^*.

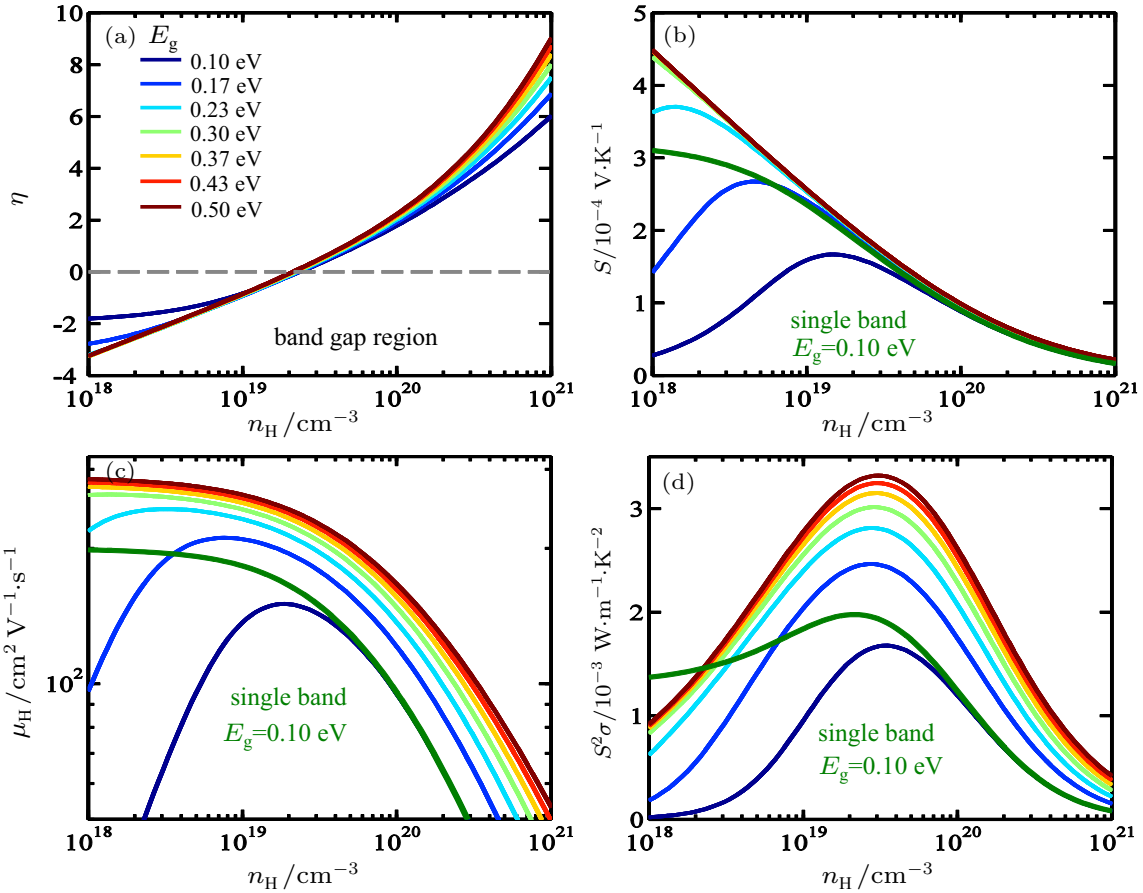


Fig. 5. (color online) (a) Determined η with n_H ranging from 10^{18} cm^{-3} to 10^{21} cm^{-3} for evenly selected seven E_g values from 0.1 eV to 0.5 eV. Correspondingly calculated (b) S, (c) μ_H, and (d) $S^2\sigma$ as a function of n_H for different E_g values.

Figure 5 shows the effects of E_g on thermoelectric properties. Firstly, with increasing n_H from 10^{18} cm^{-3} to 10^{21} cm^{-3}, the determined η for evenly selected seven E_g values from 0.1 eV to 0.5 eV is exhibited in Fig. 5(a). As can be seen, $|\eta|$ tends to

increases with increasing E_g for a given n_H. Figure 5(b) presents the plots of S as a function of n_H for different E_g values. Larger E_g produces larger S peak and shifts the peak of S to low n_H, which quantitatively verifies the effectiveness of E_g on suppressing bipolar conduction. The suppressed bipolar conduction due to large E_g is also demonstrated in the variation of μ_H (see Fig. 5(c)). Figure 5(d) shows the variations of $S^2\sigma$ with E_g, from which enlarging E_g can greatly enhance peak $S^2\sigma$ but does not change the n_H^{opt} significantly.

Lastly, we studied the impacts of E_{def} on electronic transport coefficients. Because E_{def} characterizes the strength of phonon scattering on free charge carriers,[93,94] we anticipate that E_{def} would not affect η and bipolar conduction. This has been confirmed by the determined η and the correspondingly calculated S, as shown in Figs. 6(a) and 6(b), respectively. However, small E_{def} can greatly increase μ_H (refer to Fig. 6(c)). As a consequence, small E_{def} leads to high $S^2\sigma$, which can be seen from Fig. 6(d). Interestingly, E_{def} does not change n_H^{opt}.

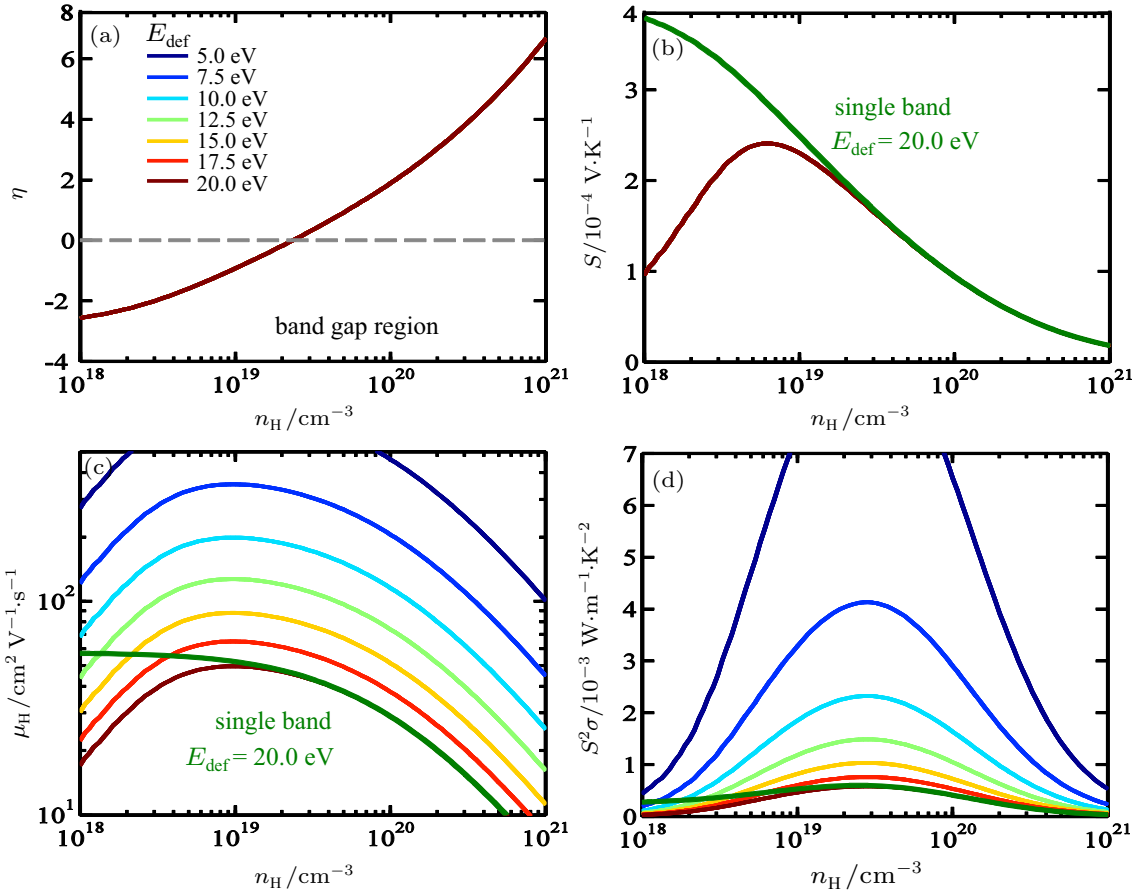


Fig. 6. (color online) (a) Determined η with n_H ranging from 10^{18} cm^{-3} to 10^{21} cm^{-3} for evenly selected seven E_{def} values from 5 eV to 20 eV. Correspondingly calculated (b) S, (c) μ_H, and (d) $S^2\sigma$ as a function of n_H for different E_{def} values. The bold green lines in panels (b) and (c) are calculated using SKB model with $E_{def} = 8$ eV for S and μ_H, respectively.

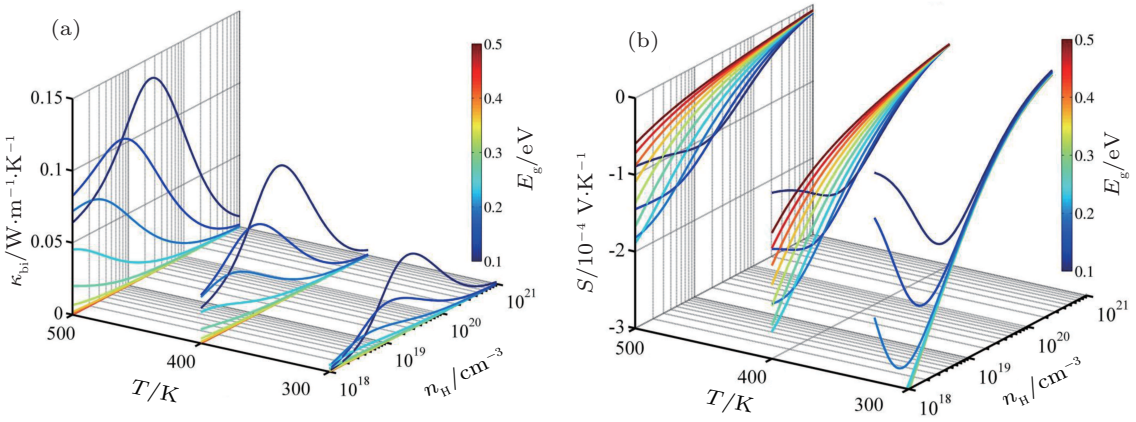


Fig. 7. (color online) Calculated (a) κ_{bi}, and (b) S as a function of n_H at 300 K, 400 K, and 500 K for evenly selected seven E_g values from 0.1 eV to 0.5 eV.

It is well documented that bipolar conduction is detrimental to the thermoelectric performance by generating κ_{bi} and reducing S. Here, we emphasized the significance of suppressing bipolar conduction by enlarging E_g. Figures 7(a) and 7(b) show the calculated κ_{bi} and S as a function of n_H for evenly selected seven E_g values from 0.1 eV to 0.5 eV. Because bipolar conduction is more notable at high temperature, the calculation covers the results at 300 K, 400 K, and 500 K. As can be seen, at high temperature, κ_{bi} is large but S is small, and enlarging E_g can greatly reduce κ_{bi} but increases S.

Based on above discussions, we can see that m_d^*, E_g, and E_{def} can significantly affect $S^2\sigma$, but only m_d^* is able to change the n_H^{opt}. To determine n_H^{opt}, we calculated $S^2\sigma$ as functions of n_H and m_d^*, shown in Fig. 8(a). Based on this, the n_H^{opt} values corresponding to different m_d^* are plot as a white curve in Fig. 8(b), in which the background is the contour plot of $S^2\sigma$ as functions of n_H and m_d^*. As can be seen, the variation of contour plot follows the white curve. To enhance thermoelectric performance, we want to ensure the experimental n_H value close to n_H^{opt}.

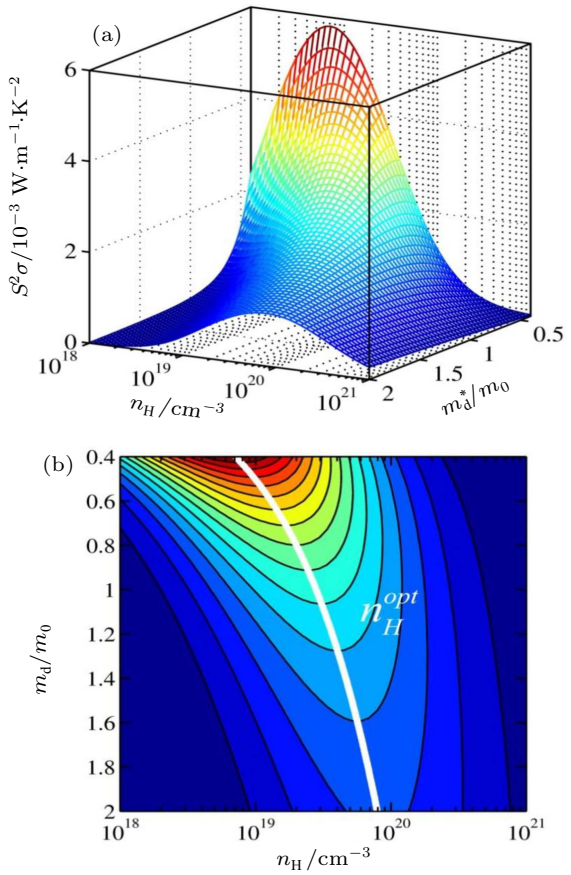


Fig. 8. (color online) (a) Calculated $S^2\sigma$ as functions of n_H and m_d^*, and (b) the corresponding contour map with the white curve indicating the m_d^*-dependent n_H^{opt}.

5. Bi_2Te_3-based thermoelectric materials

Bi_2Te_3-based materials share the same rhombohedral crystal structure of the space group $R\bar{3}m$ (see Fig. 9(a)). This category consists of five-atom layers arranged along the c axis, known as quintuple layers. The coupling is strong between two atomic layers, but is much weaker within one quintuple layer, predominantly of the van der Waals type. Lattice parameters and band gap (E_g) of these layered materials are shown in Table 1. The electronic band structures of Bi_2Te_3 are shown in Fig. 9(c) with the selected high symmetry k points shown in Fig. 9(b). As can be seen, both the highest valence band and lowest conduction band have six valleys. Besides these two bands, the second conduction and valence band with energy separations of 30 meV and 20 meV, respectively.[95]

Pnictogen (Bi and Sb) and chalcogenides (Te and Se) materials have been preferably studied for room-temperature thermoelectric applications.[70] These materials share the same rhombohedral crystal structure of the space group $R\bar{3}m$ (see Fig. 9). This category consists of five-atom layers arranged along the c axis, known as quintuple layers. The coupling is strong between two atomic layers, but is much weaker within one quintuple layer, predominantly of the van der Waals type. Lattice parameters and band gap (E_g) of these layered materials are shown in Table 1.

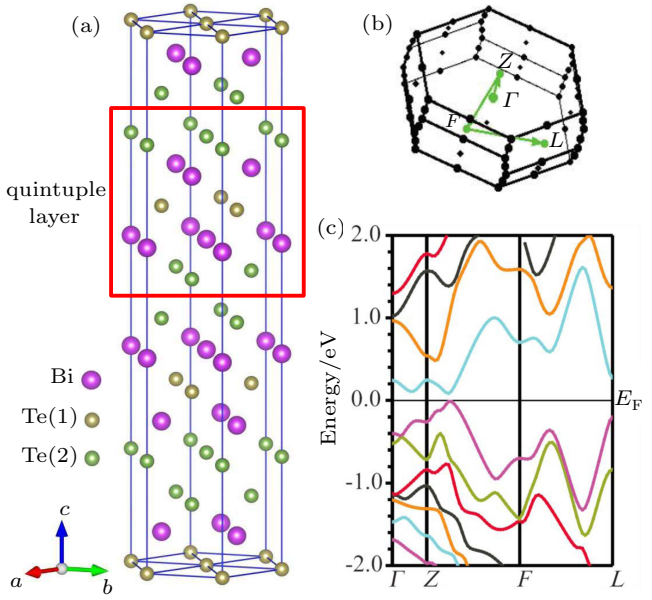


Fig. 9. (color online) (a) crystal structure, (b) first Brillouin zone, and (c) band structure. Reproduced from Ref. [96].

Table 1. Physical properties of N_2M_3(N: Bi, Sb; M: Te, Se).[97,98]

	Bi_2Te_3	Bi_2Se_3	Sb_2Te_3
Structure	hexagonal	hexagonal	hexagonal
a/Å	4.38	4.14	4.26
c/Å	30.48	28.64	30.45
Unit layer/Å	10.16	9.55	10.15
Band gap/eV	0.15	0.3	0.22

Based on above discussions, Bi_2Te_3 families crystalize in layered structures and consist of heavy atoms, which can

potentially ensure low κ. Moreover, the narrow E_g can secure a high σ, and the large band degeneracy is also beneficial to produce a high $S^2\sigma$. Because of these advantages of Bi_2Te_3 for thermoelectric applications, great efforts have been dedicated to enhancing the thermoelectric efficiencies. Table 2 summarizes the reported thermoelectric properties for both n-type Bi_2Te_3 and p-type Sb_2Te_3 based thermoelectric materials. As can be seen, zT of 1.2 has been achieved in n-type Bi_2Te_3,[99–102] and zT of 1.56 has been obtained in p-type Sb_2Te_3.[103] The big difference between the n-type and the p-type materials is mainly due to the much lower $S^2\sigma$ in Bi_2Te_3, although the obtained lowest κ of n-type Bi_2Te_3 is even smaller than that of p-type Sb_2Te_3.

Table 2. Thermoelectric properties of the Bi_2Te_3-based materials prepared by different methods.

Material	Type	$S^2\sigma/10^{-4}$ W·m^{-1}·K^{-2}	$\kappa(\kappa_l)$/W·m^{-1}·K^{-1}	zT	T/K	Method[a)]
Nanostructuring						
Bi_2Te_3[104]	n	11.9	0.46(0.25)	0.91	350	MSS+CP
$Bi_{0.5}Sb_{1.5}Te_3$[104]	P	14.9	0.45(0.25)	1.2	363	MSS+CP
$Bi_2Te_{2.7}Se_{0.3}$[105]	n	11	0.6	0.55	300	SG+SPS
$Bi_2Te_{2.7}Se_{0.3}$[106]	n	11	0.6	0.54	300	SG+SPS
$Bi_{0.5}Sb_{1.5}Te_3$[38]	p	28	0.7(0.4)	1.2	320	MSS+SPS
$Bi_{0.4}Sb_{1.7}Te_{3.0}$[107]	p	9	0.35(0.16)	0.9	413	SG+SPS
$(Bi_2Te_3)_{0.85}(Bi_2Se_3)_{0.15}$[108]	n	12	0.68(0.45)	0.71	480	SG+SPS
$(Bi_2Te_3)_{0.8}(Bi_2Se_3)_{0.2}$[109]	n	9	0.53(0.38)	0.71	450	SG+SPS
$Bi_{0.5}Sb_{1.5}Te_3$[110]	p	24	0.66(0.3)	1.13	360	MSS+SPS
Bi_2Te_3[111]	n	15.4	1.1	0.66	470	SG+HP
Bi_2Te_3-Te[112]	n	18.7	1.22(0.45)	0.6	390	SG+HP
Bi_2Te_3[35]	n	6.9	0.45(0.28)	0.62	400	SG+SPS
Bi_2Se_3[113]	n	4.4	0.42	0.35	400	LIE+HP
Bi_2Se_3[114]	n	4.7	0.41(0.3)	0.48	425	MSS+SPS
S doped Sb_2Te_3[115]	p	20.0	0.7(0.35)	0.95	423	MSS+CP
Bulk materials						
Bi_2Te_3[116]	p	20	0.78(0.36)	1.03	403	HPS
Bi_2Se_3[117]	n	6	0.97(0.4)	0.37	560	HPS
$Bi_{0.5}Sb_{1.5}Te_3$[70]	p	44	1	1.4	373	BM+HP
$Bi_{0.5}Sb_{1.5}Te_3$[118]	p	43	1	1.3	373	BMA+HP
$Bi_2Te_{2.7}Se_{0.3}$[119]	n	26	1.08	1.04	400	BMA+HP
Bi_2Te_3[102]	n	33	1.1	1.2	425	BMA+HP
$Bi_{0.5}Sb_{1.5}Te_3$[120]	p	38	0.85(0.48)	1.4	300	MA+HP
$Bi_2Te_{2.79}Se_{0.21}$[99]	n	42	0.8(0.56)	1.2	357	HP
$Bi_2Te_{2.3}Se_{0.7}$[100]	n	28	1.1(0.4)	1.2	445	MA+BM+HP
$Bi_{0.3}Sb_{1.7}Te_3$[100]	p			1.3	380	MA+BM+HP
$Bi_2Te_{2.925}Se_{0.075}$[121]	n	47	1.65(1.27)	0.85 (a–b)	293	THM
$Bi_{0.52}Sb_{1.48}Te_3$[103]	p	35	0.65(0.25)	1.56	300	MS
$Cu_{0.01}Bi_2Te_{2.7}Se_{0.3}$[122]	n	31.2	1.1	1.06	373	BM+HP
$Bi_2Te_{2.7}Se_{0.3}$[101]	n	53.8	1.87	1.18	410	BS
$Bi_2(Te_{1-x}Se_x)_3$-I(0.08%)[123]	n	55	1.5(0.9)	1.1	340	ZM
$Bi_2(Te_{0.5}Se_{0.5})_3$-I 0.1%[123]	n	25	1.42(0.45)	0.85	570	ZM

[a)] The abbreviations used in the column of preparation method represent the following meanings: MSS = microwave solvothermal, CP = cold pressing, SG = solution grow, SPS = spark plasma sintering, HP = hot pressing, LIE = lithium ionic exfoliation, BMA = ball milling alloy, MA = melting alloy, HPS = high pressure synthesis, BS = Bridgman–Stockbarger, BM = ball milling, THM = travelling heater method, MS = melt spinning, Te-MS = Te-rich melt spinning, ZM = zone melting.

6. The characteristics of Bi_2Te_3 families as thermoelectric applications

6.1. Intensive bipolar conduction at relatively high temperature

Bipolar conduction is the excitation of minor charge carriers. In n-type semiconductors (as an example), electrons are thermally excited from the valence band to the conduction band, leaving behind holes as the minor charge carriers in the valance, as illustrated by the schematic diagram of Fig. 10.[124] Since electrons and holes have opposite charges, the total S is offset if both electrons and holes are present, refer to Fig. 3(b). For semiconductors, S increases with elevating temperature, and the turn-over of S is caused by the bipolar conduction.[124,125] Because the existence of bipolar conduction is related to the band gap (E_g), the Goldsmid–Sharp relation (i.e., $E_g = 2eS_{max}T$ with S_{max} and T representing the

peak value of S and the corresponding temperature, respectively) was proposed to roughly estimate E_g according to the variation of S with temperature.[126] Later on, a more precise method by taking into account the different weighted carrier mobility ratios between balance band and conduction was proposed to estimate E_g based on temperature-dependent S.[127] Despite the detrimental effect on S, the minor charge carriers also contribute to κ_{bi}, which has been quantitatively studied previously as shown in Fig. 3(f) and Fig. 7(a). Although κ_{bi} is lower than κ_e and κ_l in most cases, the high-temperature zT is sensitive to κ_{bi}. Based on above discussion, we can see that the suppression of bipolar conduction can enhance the overall zT from two aspects — shifting the peak of S to high temperature and reducing κ.

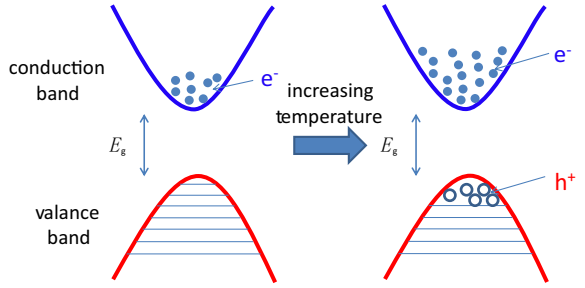


Fig. 10. (color online) Schematic diagram illustrating the bipolar conduction.

As demonstrated in Table 1, Bi_2Te_3 families are semiconductors with narrow E_g. Consequently, bipolar conduction is prominent at relatively high temperature, which deteriorates their performance. Thereby, it is necessary to suppressing bipolar conduction, which will be discussed in Section 7.

6.2. Anti-site defects and vacancies

For Bi_2Te_3, the most common defects are vacancies at Te sites and anti-site defects of Bi in Te-sites.[128] The formation of vacancies is caused by the evaporation of consisting elements,[122] and the motivation of anti-site defects is the differences of electronegativity and atomic size between Te and Bi.[129] The formation of Te vacancies (assuming x-mol from 1-mol Bi_2Te_3) follows

$$Bi_2Te_3 \rightarrow 2Bi_{Bi}^{\times} + (3-x)\,Te_{Te}^{\times} + xTe\,(g)\uparrow + xV_{Te}^{2+} + 2xe^{-}. \tag{51}$$

On the basis of x-mol V_{Te}^{2+} in 1-mol Bi_2Te_3, the generation of y-mol anti-site defects of Bi at Te site can be expressed as

$$\begin{aligned} Bi_2Te_3 \rightarrow\ & (2-z)\,Bi_{Bi}^{\times} + zBi_{Te}^{-} + (3-x)\,Te_{Te}^{\times} + xTe\,(g)\uparrow \\ & + (x-z)\,V_{Te}^{2+} + 2xe^{-} + 3zh^{+}. \end{aligned} \tag{52}$$

In the above equations, $Bi_{Bi}^{\times}$ and $Te_{Te}^{\times}$ are Bi and Te atoms at their original sites in the lattice, Te(g) is the evaporation of Te, V_{Te}^{2+} is the Te vacancies, and Bi_{Te}^{-} is the anti-site defect of Bi at Te site, respectively. From Eqs. (51) and (52), we can see that V_{Te}^{2+} is positively charged, and one V_{Te}^{2+} contributes two electrons, whereas Bi_{Te}^{-} is negatively charged, and one Bi_{Te}^{-} gives one hole. Most Bi_2Te_3 single crystals or ingots with coarse grains are intrinsically p-type because Bi_{Te}^{-} is the dominating defects. For fine-grained polycrystalline samples and nanostructures, the dangling bonds at grain boundaries due to Te deficiencies can also be considered as fractional V_{Te}^{2+}, therefore more V_{Te}^{2+} is generated, suggesting fine-grained polycrystalline samples and nanostructures are generally n-type.[122]

Likewise, in Bi_2Se_3, Sb_2Se_3, and Sb_2Te_3, there also exist positively charged anion vacancies of V_{Te}^{2+}, and V_{Se}^{2+}, as well as negatively charged anti-site defects of Bi_{Se}^{-}, Sb_{Se}^{-}, and Sb_{Te}^{-}. The formation of anion vacancies depends on the evaporation heat, and the formation of anti-site defects rely on the differences of electronegativity and covalent radius between the consisting cation and anion atoms. Table 3 lists the parameters of evaporation heat, electronegativity and ionic radius of Te, Se, Bi, and Sb. As can be seen, V_{Se}^{2+} is more easily to happen than V_{Te}^{2+}, and the formation of anti-site defects follows the sequence (easy to difficult) of Sb_{Te}^{-}, Bi_{Te}^{-}, Sb_{Se}^{-}, and Bi_{Se}^{-}. That is why single crystal Sb_2Te_3 is degenerated p-type semiconductor, Bi_2Te_3 is nearly intrinsic p-type, and Bi_2Se_3 is degenerate n-type, respectively.

Table 3. The electronegativity and evaporation heat for Te, Se, Bi, and Sb.

	Te	Se	Bi	Sb
Evaporation heat/kJ·mol^{-1}[130]	52.55	37.70	104.8	77.14
Electronegativity[129]	2.1	2.55	2.02	2.05
Covalent radius/Å[130]	127.6	78.96	208.98	121.75

The existence of defects can also enhance the scattering of phonons with high frequency due to the mass fluctuation and strain.[131] However, defects make it hard to tune the thermoelectric properties and lead to the irreproducibility of the obtained high thermoelectric properties.[122] For the nanostructures and ball milling samples, there are more anion vacancies due to the dangling bonds in the dense grain boundaries. Unfortunately, the number of anion vacancies cannot be well controlled.

6.3. Strong anisotropic behavior

Bi_2Te_3 crystal has remarkable anisotropy that originates from the layered rhombohedral structure. Specifically, the σ and κ in a–b plane (perpendicular to the c axis) are about four and two times, respectively, larger than those along the c axis in Bi_2Te_3.[102] The S shows the only slight difference with respect to anisotropy. So, zT in the a–b plane is approximately

two times as large as that along the c axis, as shown in Table 4.[121] On the contrary, thermoelectric properties of Sb_2Te_3 single crystal exhibit weaker anisotropic behavior, and the zT values along the two perpendicular directions are nearly identical.

Table 4. The anisotropic behavior of single crystals of Bi_2Te_3 families.

	$\sigma_{\perp c}/\sigma_{\|\|c}$	$S_{\perp c}/S_{\|\|c}$	$(S^2\sigma)_{\perp c}/(S^2\sigma)_{\|\|c}$	$\kappa_{\perp c}/\kappa_{\|\|c}$	$zT_{\perp c}/zT_{\|\|c}$
$Bi_2Te_{2.6}Se_{0.4}$[121]	4.38	1.03	4.65	2.15	2.17
$Bi_{0.5}Sb_{1.5}Te_3$[132]	2.65	1.02	2.75	1.93	1.42

In most cases, we use nanostructuring or ball milling to reduce the grain size for obtaining a significantly reduced κ. However, this would simultaneously deteriorate $S^2\sigma$ to some extent, resulted from the random crystal orientation. Since Bi_2Te_3 shows stronger anisotropic behavior than Sb_2Te_3, while the state-of-the-art zT is only ~ 1.2[100] for Bi_2Te_3-based materials, zT in polycrystalline Sb_2Te_3-based materials can be up to 1.56[103] because of the dramatically reduced κ and the preserved high $S^2\sigma$ (refer to Table 2).

7. Strategies for enhancing thermoelectric performance of Bi_2Te_3 families

Based on the summarized feature of Bi_2Te_3 families, some strategies have been developed to enhance the thermoelectric performance. In fact, these strategies are combined together to achieve a higher zT.

7.1. Suppressing bipolar conduction

As discussed in Section 4, increasing E_g is effective to suppress bipolar conduction. Forming ternary phases of $Bi_2Te_{3-x}Se_x$ and $Bi_xSb_{2-x}Te_3$ can tune E_g. Figure 11(a) shows the E_g for $Bi_2Te_{3-x}Se_x$ with different compositions. With increasing Se content, E_g for $Bi_2Te_{3-x}Se_x$ increases until $x = 1$, and then decreases. The reason for the variation of E_g with Se content is due to the chemical bonding environment and the electronegativity difference. As demonstrated earlier, Bi_2Te_3 consists of quintuple layers, in which the atoms are arranged in the order of Te(1)–Bi–Te(2)–Bi–Te(1) with two types of differently bonded Te atoms.[133] While chemical bonding between Bi–Te(2) is pure covalent, it is slightly ionic but still covalent in nature between Bi–Te(1), suggesting the bonding between Bi–Te(1) is stronger.[134] To form $Bi_2Te_{3-x}Se_x$, Se atoms firstly substitute Te at Te(2) sites. When $x > 1$, Se further goes to Te(1) sites randomly. Owing to Se being more electronegative than Te (refer to Table 3),[129] the chemical bonding of Bi–Se is stronger than Bi–Te(2), which enables electrons in $Bi_2Te_{3-x}Se_x$ being more localized. It is understood that with increasing x from 0 to 1 in $Bi_2Te_{3-x}Se_x$, E_g increases. Thereafter, E_g tends to decrease with further increasing $x > 1$, because Se may weaken Bi–Te(1) bonding.

For $Bi_xSb_{2-x}Te_3$ with an electronegativity of Bi slightly less than that of Sb, it is understood that with increasing Sb content, E_g increases, as depicted in Fig. 11.

Noteworthy, it is well documented that the optimal compositions corresponding to the peak zT values are $Bi_2Te_{2.7}Se_{0.3}$, and $Bi_{0.5}Sb_{1.5}Te_3$, in which E_g values are not the highest.[135] To increase zT, we should simultaneously control the band structures (including E_g, m_b^*, and E_f) and phonon scatterings. Among these strategies, enlarging E_g is still a critical factor in $Bi_2Te_{2.7}Se_{0.3}$, and $Bi_{0.5}Sb_{1.5}Te_3$ to achieve higher zT than their respective binary phases.

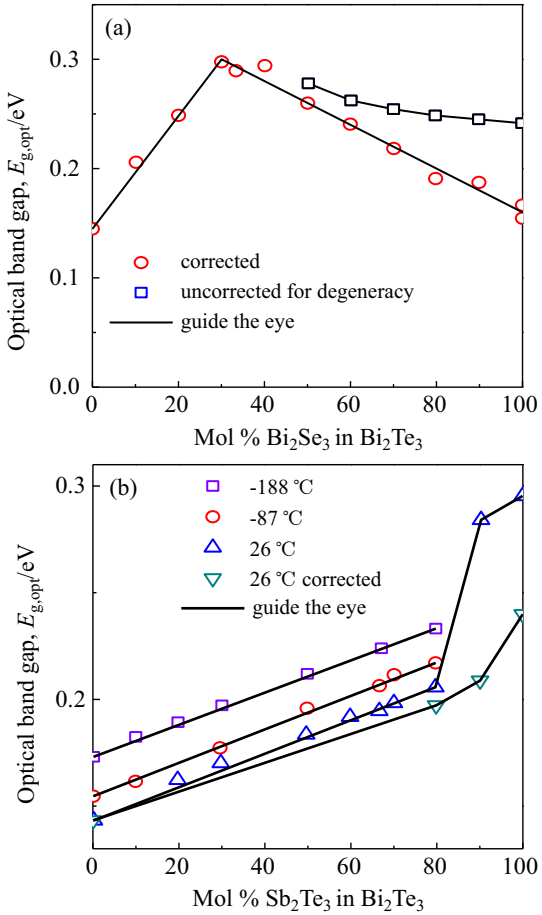


Fig. 11. (color online) Composition-dependent E_g of (a) $Bi_2Te_{3-x}Se_x$ and (b) $Bi_xSb_{2-x}Te_3$. Reproduced from Refs. [136] and [137].

Moreover, reducing the size of nanostructures can also increase E_g due to the quantum confinement effect.[138–140] For example, it has been confirmed that E_g of Bi_2Se_3 nanosheets with a thickness of 1 nm is ~ 0.85 eV, much higher than that of 0.3 eV for the bulk counterpart.[141] Consequently, reducing the thickness of Bi_2Se_3 nanosheets can enhance the thermoelectric performance. Experimentally, zT of Bi_2Se_3 nanosheets with 1 nm was enhanced to be over 0.3.

In respect of suppressing the bipolar conduction, we can also introduce potential barriers to resist the transport of minor carriers. Considering the band alignment between Bi_2Te_3 and Bi_2Se_3, potential barriers of 0.26 eV in the valence band and 0.11 eV in the conduction band of the n-type Bi_2Te_3/Bi_2Se_3 could be formed.[142] In this scenario, the transport of excited minor carriers (holes) in the valance band could be resisted.[76] Combined with the energy filtering effect on the major carriers in the conduction band, thermoelectric performance of the n-type Bi_2Te_3/Bi_2Se_3 was enhanced significantly.[108] Moreover, increasing the carrier concentration to push E_f away from the band gap region can also be effective to suppress bipolar conduction, because the bipolar effect is the strongest in the band gap region (refer to Figs. 3(b) and 3(f)). In nanostructures prepared by solution or ball milling methods, more point defects would be formed, which results in higher carrier concertation.[100] Therefore, we can observe that in these products, the peak zT generally occurs at relatively high temperature.[102,112,122,143,144]

7.2. Point defect engineering

As mentioned previously, point defects unavoidably present in Bi_2Te_3 families, and significantly affect the thermoelectric properties. On one hand, the anion vacancies and antisite defects serve as donors and acceptors, respectively, to determine the carrier type and carrier concentration. On the other hand, point defects, leading to the mass fluctuations and lattice strains, can enhance the scattering of high-frequency phonons to reduce κ.[131] In this regard, it is necessary to control the inherent vacancies and antisite defects by point defect engineering. The effective methods are mainly to form the ternary phases (i.e., n-type $Bi_2Te_{3-x}Se_x$ and p-type $Bi_xSb_{2-x}Te_3$), and doping. In this section, we focus on the effect of point defects on electronic transport. Note that the smaller evaporation energy leads to the easier formation of vacancies, and the smaller differences of electronegativity and atomic size motivate the formation of antisite defects.[145] From Table 3, the point defects strongly depend on the composition of $Bi_2Te_{3-x}Se_x$ and $Bi_xSb_{2-x}Te_3$. Specifically, increasing Se content in $Bi_2Te_{3-x}Se_x$ increases anion vacancies but decreases antisite defects, and increasing Bi content in $Bi_xSb_{2-x}Te_3$ can suppress antisite defects but does not notably affect the anion vacancies.

To clarify the effects of point defects on electronic transport, we summarized the reported data for these ternary phases. Figure 12 summarized n_H, μ_H, σ, and S at 300 K for the representative n-type $Bi_2Te_{3-x}Se_x$ single crystal,[146] single crystal doped with Ag (0.1%),[146] hot pressing plus hot deformation (BM+HP+HD) processed sample,[100] and ingot doped with I (0.08 wt%).[123] From Fig. 12(a), with increasing

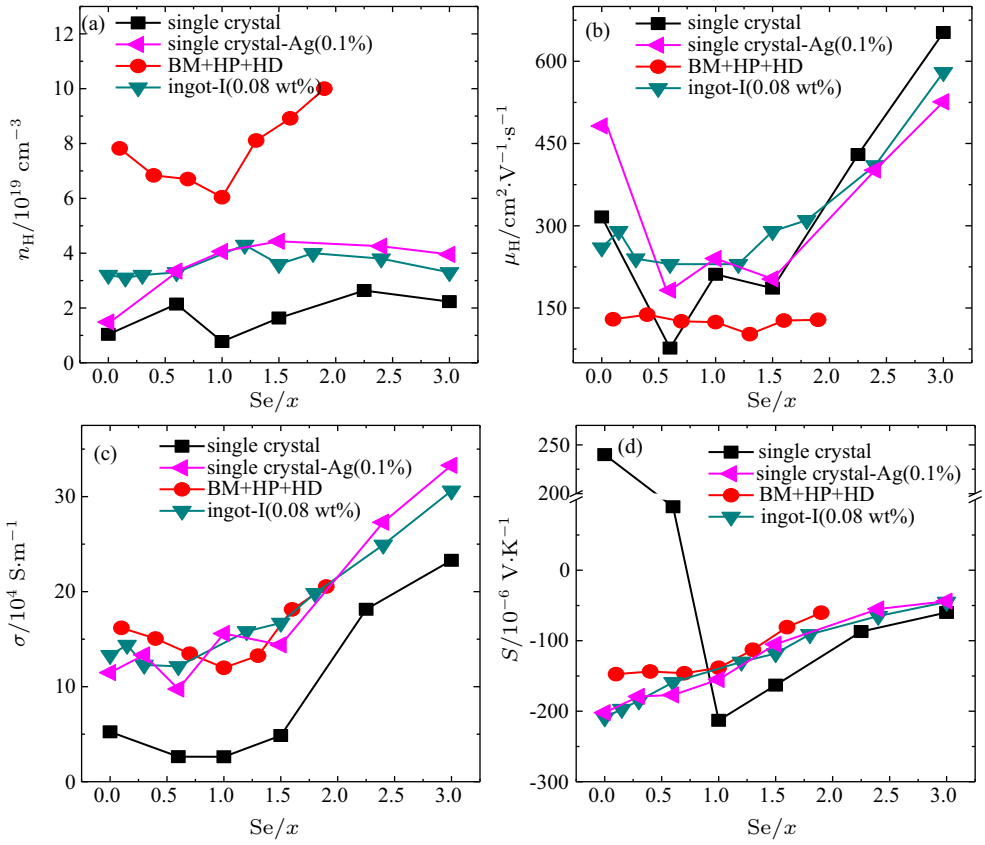


Fig. 12. (color online) n-type $Bi_2Te_{3-x}Se_x$ with (a) n_H, (b) μ_H, (c) σ, and (d) S at 300 K as a function of Se content for single crystal,[146] single crystal doped with Ag (0.1%),[146] BM+HP+HD processed sample,[100] and ingot doped with I (0.08 wt%).[123]

Se content in $Bi_2Te_{3-x}Se_x$, n_H for the single crystals and the ingot gently increases, whereas n_H for the samples prepared by BM+HP+HD initially decreases and then increases. The general increasing trend of n_H with increasing Se content is ascribed to the increase in anion vacancies dominating over that of antisite defects. The decrease in n_H for the BM+HP+HD processed samples with low Se content is caused by the antisite defects exhibiting a stronger effect on carrier concentration over vacancies. From Fig. 12(b), μ_H for single crystals and ingot show intensive fluctuations, while that for BM+HP+HD processed samples stabilize at a plateau, which means the effects of point defects on μ_H also depends on the sample preparation methods. Because of the variation of n_H and μ_H caused by point defects, σ and S are modified, shown in Figs. 12(c) and 12(d), respectively. While σ generally increases with increasing Se content, S decreases. Based on the discussion in Section 4, large n_H means high η, resulting in high σ but low S. Moreover, in the pristine $Bi_2Te_{3-x}Se_x$ single crystal with lower n_H (black data points), its S transfers from p-type to n-type with increasing Se content, suggesting the major carriers change from holes to electrons. This is because the Bi_2Te_3 single crystal is a nearly intrinsic p-type semiconductor, whereas substituting Te in the lattice of Bi_2Te_3 single crystal with Se atoms can increase anion vacancies contributing more electrons, which produces the transition from p-type to n-type.

Figure 13 presents the effect of Bi content on electronic transport properties for the typical p-type $Bi_xSb_{2-x}Te_3$ single crystals[132] and BM+HP+HD processed analogs.[100] With increasing Bi content, n_H increases, whereas μ_H generally decreases. As a consequence, σ increases, whereas S generally decreases.

In addition, doping can also modify the point defects. S-doped Sb_2Te_3 can reduce the antisite defects to reduce the carrier concentration and diminish the impurity scattering on holes to enhance the carrier mobility.[115] Another case is Cu-doped $Bi_2Te_{2.7}Se_{0.3}$, which can reduce the vacancies to enhance the carrier mobility.[122] We also noted that hot deformation can reduce the anion vacancies to decrease n_H for the sintered polycrystalline samples. For example, n_H for Bi_2Te_3 was reduced to only 1.5×10^{19} cm^{-3} by hot deformation at 733 K, compared with that of 5.9×10^{19} cm^{-3} in the unprocessed counterpart, and as a consequence, S increased from -116 μV·K^{-1} to -141 μV·K^{-1}.[99,100]

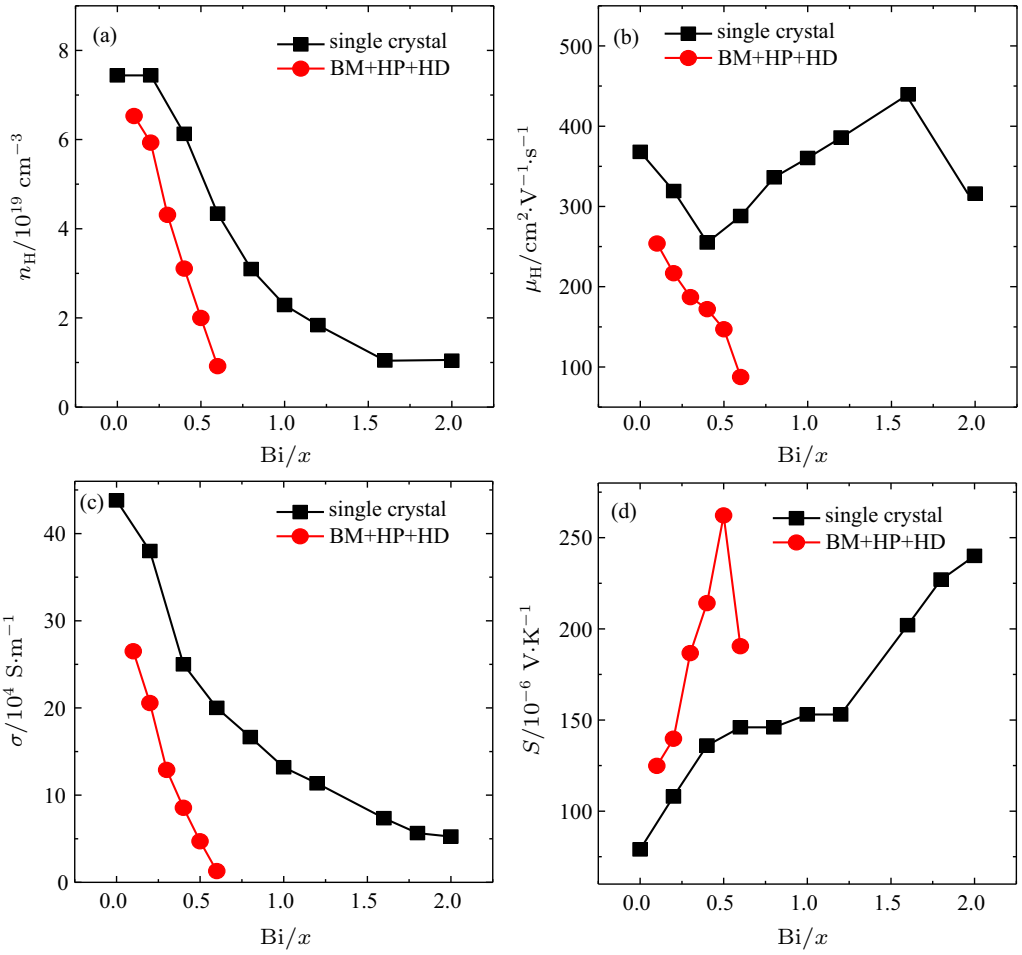


Fig. 13. (color online) p-type $Bi_xSb_{2-x}Te_3$ with (a) n_H, (b) μ_H, (c) σ, and (d) S at 300 K as a function of Bi content for single crystal,[132] and BM+HP+HD processed sample.[100]

7.3. Crystalline alignment

Compared with single crystal Bi_2Te_3, polycrystalline materials are promising to realize practical applications, which is due to (i) stronger mechanical strength[147] and (ii) dense grain boundaries to reduce κ.[37] Nevertheless, the strong anisotropic behavior of Bi_2Te_3 would worsen $S^2\sigma$ in polycrystalline materials. Therefore, crystalline alignment (i.e., enhancing the texture) is likely to enhance zT for polycrystalline samples.[148] Hot deformation is widely used to enhance the texture of Bi_2Te_3 families.[149] Figure 14 summarizes the cutting-edge thermoelectric performance of both n-type $Bi_2Te_{3-x}Se_x$ and p-type $Bi_xSb_{2-x}Te_3$ benefiting from the hot deformation to enhance the texture of the sintered samples. For n-type ones, σ is enhanced significantly after hot deformation, while the enhancement of S caused by hot deformation is not so significant. Overall, $S^2\sigma$ for the n-type $Bi_2Te_{3-x}Se_x$ is elevated dramatically after hot deformation, which leads to enhanced zT. For p-type $Bi_xSb_{2-x}Te_3$, hot deformation does not affect $S^2\sigma$ notably but can reduce κ to some extent. For this reason, zT of p-type candidates can also be enhanced. On this basis, hot deformation enhances zT for n-type $Bi_2Te_{3-x}Se_x$ and p-type $Bi_xSb_{2-x}Te_3$ from different aspects: enhancing $S^2\sigma$ and reducing κ, respectively.

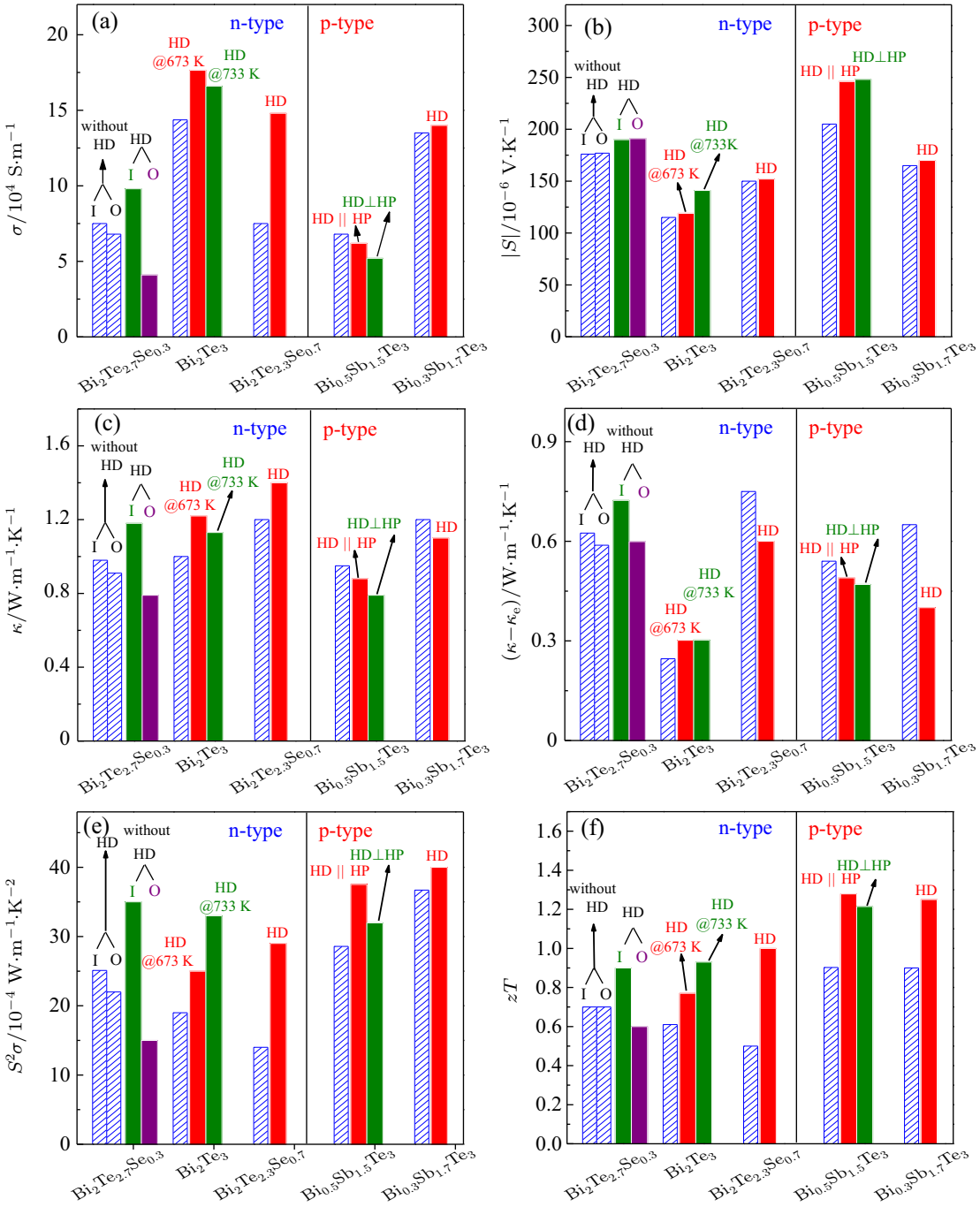


Fig. 14. (color online) The effects of hot deformation on reported (a) σ, (b) S, (c) κ, (d) κ_l (e) $S^2\sigma$, and (f) zT for n-type $Bi_2Te_{2.7}Se_{0.3}$,[119] Bi_2Te_3,[102] $Bi_2Te_{2.3}Se_{0.7}$,[100] and p-type $Bi_{0.5}Sb_{1.5}Te_3$,[120] $Bi_{0.3}Sb_{1.7}Te_3$.[100]

7.4. Enhancing phonon scattering

Enhancing phonon scattering to reduce κ is also effective to enhance the final zT. Despite the point defect scattering and hot deformation, which can reduce κ (as discussed above), we will cover other strategies for reducing κ.

7.4.1. Nanostructuring

A variety of 1D, 2D, and 3D nanostructures of Bi_2Te_3 have been synthesized by the solution grow method, including nanowires,[36,150] T-shaped Bi_2Te_3-Te heteronanojunctions,[143] Te/Bi_2Te_3 nanostring-cluster hierarchical nanostructures,[151–153] hexagonal nanoplates,[106,151,154] Bi_2Se_3 ultrathin nanosheets,[113,114,133] Bi_2Te_3/Bi_2Se_3 multishell nanoplates,[109] and 3D nanoflowers.[108,155] In the synthesis of nanostructures, surfactants are generally used to control the morphology. However, the residuals of surfactants are detrimental to the final thermoelectric performance. Therefore, it is necessary to remove the surfactants or employ the synthesis without any surfactant.

Because of the enhanced phonon scatterings in the nanostructures, κ is reduced. Figures 15(a) and 15(b) show the temperature-dependent κ and $\kappa - \kappa_e$ for $Bi_{0.5}Sb_{1.5}Te_3$ nanoplates,[38] $Bi_2Te_{2.7}Se_{0.3}$ nanoplates,[38] Bi_2Se_3 ultrathin nanosheets,[114] Bi_2Te_3/Bi_2Se_3 nanoflowers,[108] and Bi_2Te_3 nanoplates,[35] compared with the ingot.[123] As can be seen, κ of nanostructures can be less than half of the ingot.

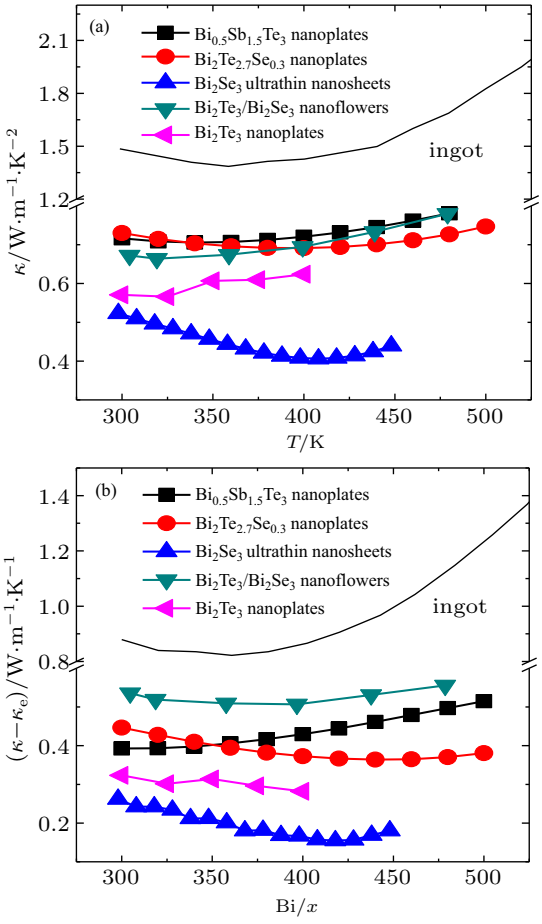


Fig. 15. (color online) (a) κ, and (b) $\kappa - \kappa_e$ for $Bi_{0.5}Sb_{1.5}Te_3$ nanoplates,[38] $Bi_2Te_{2.7}Se_{0.3}$ nanoplates, Bi_2Se_3 ultrathin nanosheets,[114] Bi_2Te_3/Bi_2Se_3 nanoflowers,[108] and Bi_2Te_3 nanoplates,[35] compared with the ingot.[123]

7.4.2. Ball milling

Ball milling can reduce the grain size so as to enhance the grain boundary scattering on phonons. Ball milling generally includes two methods: grounding the ingot with final product phase to obtain fine powders and forming pure phase by high-energy mechanical allying. Both techniques of ball milling have been successfully used to enhance zT for Bi_2Te_3 families.[156]

7.4.3. Melt spinning

Melt spinning (MS) can also significantly reduce κ. Figure 16 summarizes the thermoelectric performance of p-type $Bi_{0.5}Sb_{1.5}Te_3$ prepared by MS.[103,157,158] As can be seen, MS can reduce κ by 34% compared with the corresponding ingot and lattice component ($\kappa - \kappa_e$) could be even lower.

In the case of n-type ones, MS failed to effectively reduce κ. Ivanova *et al.* employed MS to prepare n-type $Bi_2Te_{2.7}Se_{0.3}$ alloys, but κ was not significantly reduced, which resulted in a zT similar to its ingot.[159]

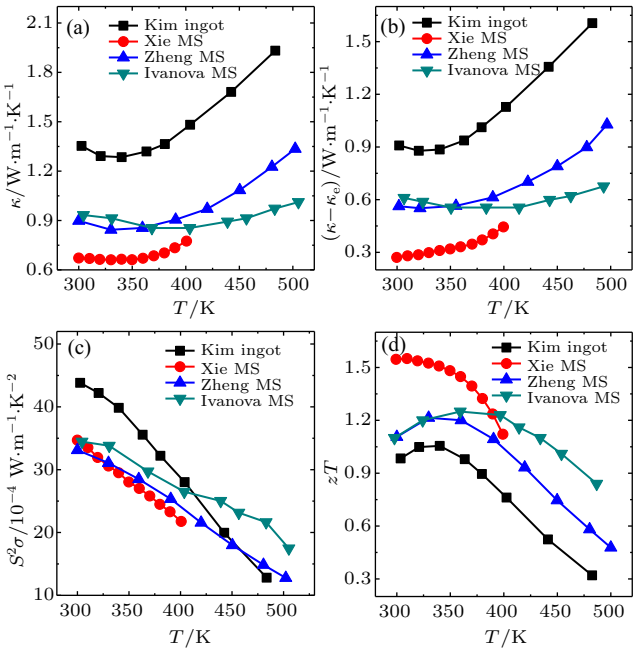


Fig. 16. (color online) (a) κ, (b) κ_l, (c) $S^2\sigma$, and (d) zT for $Bi_{0.5}Sb_{1.5}Te_3$ ingot,[160] Xie MS,[103] Zheng MS,[157] and Ivanova MS.[158]

Because thermoelectric properties are correlated with each other, we must employ multi-strategies to enhance thermoelectric performance.[161] Thermoelectric properties are related to the electronic band structure, charge carrier scattering, and phonon scattering. For a specific case with enhanced zT values, it is always due to the combination of multi-strategies

to achieve the compromise in these parameters so as to realize a net increase in zT.

8. Quantitatively understanding the reported thermoelectric properties

Based on above modeling studies, we will combine the results with the reported thermoelectric properties for Bi_2Te_3-based materials to understand the underlying reasons and provide extra hints for further enhancing their performance.

8.1. Underlying reasons for the anisotropy behavior of Bi_2Te_3 families

Crystallographically, the anisotropy behavior of Bi_2Te_3 families is caused by the layered structure. Here, we revealed the underlying fundamentals based on the reported data for single crystals. Figures 17(a) and 17(b) show the data points of S and μ_H versus n_H for n-type $Bi_2Te_{3-x}Se_x$ single crystals, respectively.[121] The curves are theoretical plots of S and μ_H as a function of n_H calculated with the determined m_d^* for S versus n_H, and E_{def} for μ_H versus n_H. The bold lines correspond to the fitted average values of m_d^* and E_{def}. Likewise, figures 17(c) and 17(d) present the analysis results for p-type $Bi_xSb_{3-x}Te_3$ single crystals.[132] From Figs. 17(a) and 17(c), the data points of S versus n_H for both n-type and p-type generally locate near the bold lines, which suggests that the difference of along the *ab* plane and the *c* axis is small. From Figs. 17(b) and 17(d), the data points of μ_H versus n_H along the two directions locate near different calculated bold lines.

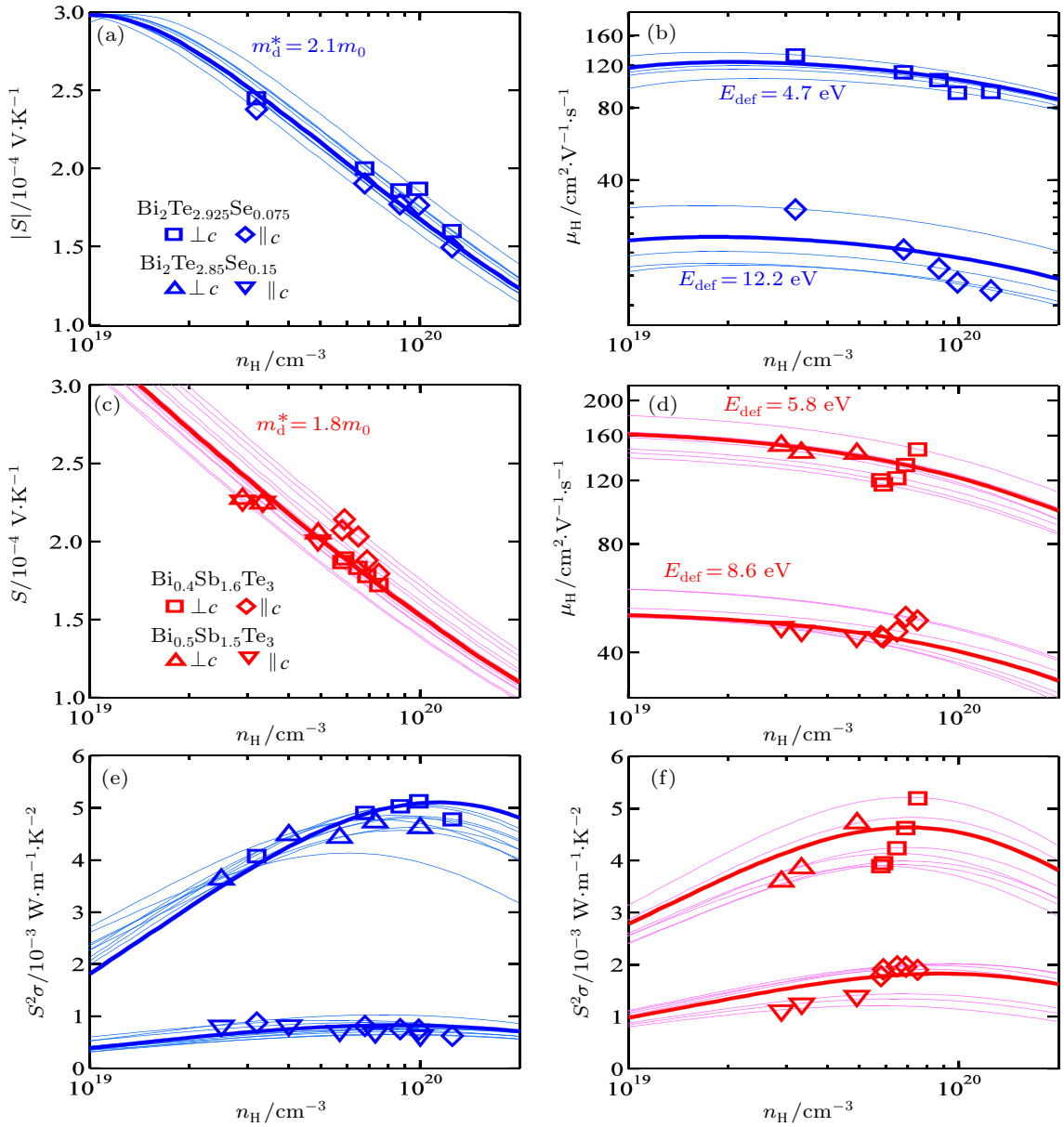


Fig. 17. (color online) (a) Data points of $|S|$ versus n_H compared with the calculated n_H-dependent $|S|$ curves, and (b) data points of μ_H versus n_H compared with the calculated n_H-dependent μ_H curves for n-type $Bi_2Te_{3-x}Se_x$ single crystals.[121] (c) Data points of S versus n_H compared with the calculated n_H-dependent S curves and (d) data points of μ_H versus n_H compared with the calculated n_H-dependent μ_H curves for p-type $Bi_xSb_{3-x}Te_3$ single crystals.[132] (e) and (f) Data points of $S^2\sigma$ versus n_H compared with the calculated n_H-dependent $S^2\sigma$ curves for n-type $Bi_2Te_{3-x}Se_x$ single crystals[121] and p-type $Bi_xSb_{3-x}Te_3$ single crystals,[132] respectively.

Therefore, the E_{def} values are significantly different along the two directions, and most importantly, such difference in E_{def} values is even larger in n-type cases. Figures 17(e) and 17(f) show the data points of $S^2\sigma$ versus n_H and the corresponding theoretical curves for n-type and p-type ones, respectively. As can be seen, the $S^2\sigma$ along the *ab* plane is larger than that along the *c* axis, and such anisotropy is stronger for n-type materials.

Based on above discussion, we concluded that the significantly different E_{def} along *ab* plane and *c* axis is responsible for the strong anisotropic σ, and the nearly identical m_d^* leads to the similar *S* along different directions. In n-type case, the difference of E_{def} along the two perpendicular directions is larger than that of p-type ones, therefore, anisotropy in n-type is even stronger.

8.2. Understanding the enhanced performance of ternary phases

As discussed above, the enhancement in thermoelectric performance for ternary phases may be caused by the enlarged E_g and point defect engineering. Here, we studied the fundamental reasons for the achieved enhancement in $S^2\sigma$ for the reported n-type $Bi_2Te_{3-x}Se_x$. Figure 18(a) is the reported Se content-dependent data points of n_H for $Bi_2Te_{3-x}Se_x$ ingots doped with I (wt 0.08%) (solid green data points),[123] $Bi_2Te_{3-x}Se_x$ processed by BM+HP+HD (hollow red data points),[100] and $Bi_2Te_{3-x}Se_x$ single crystals (hollow blue data points).[121] Considering the reported n_H, *S*, and μ_H data, we determined η, m_d^*, and E_{def} for all compositions using the Kane band model with CB and VB, shown in Figs. 18(b),

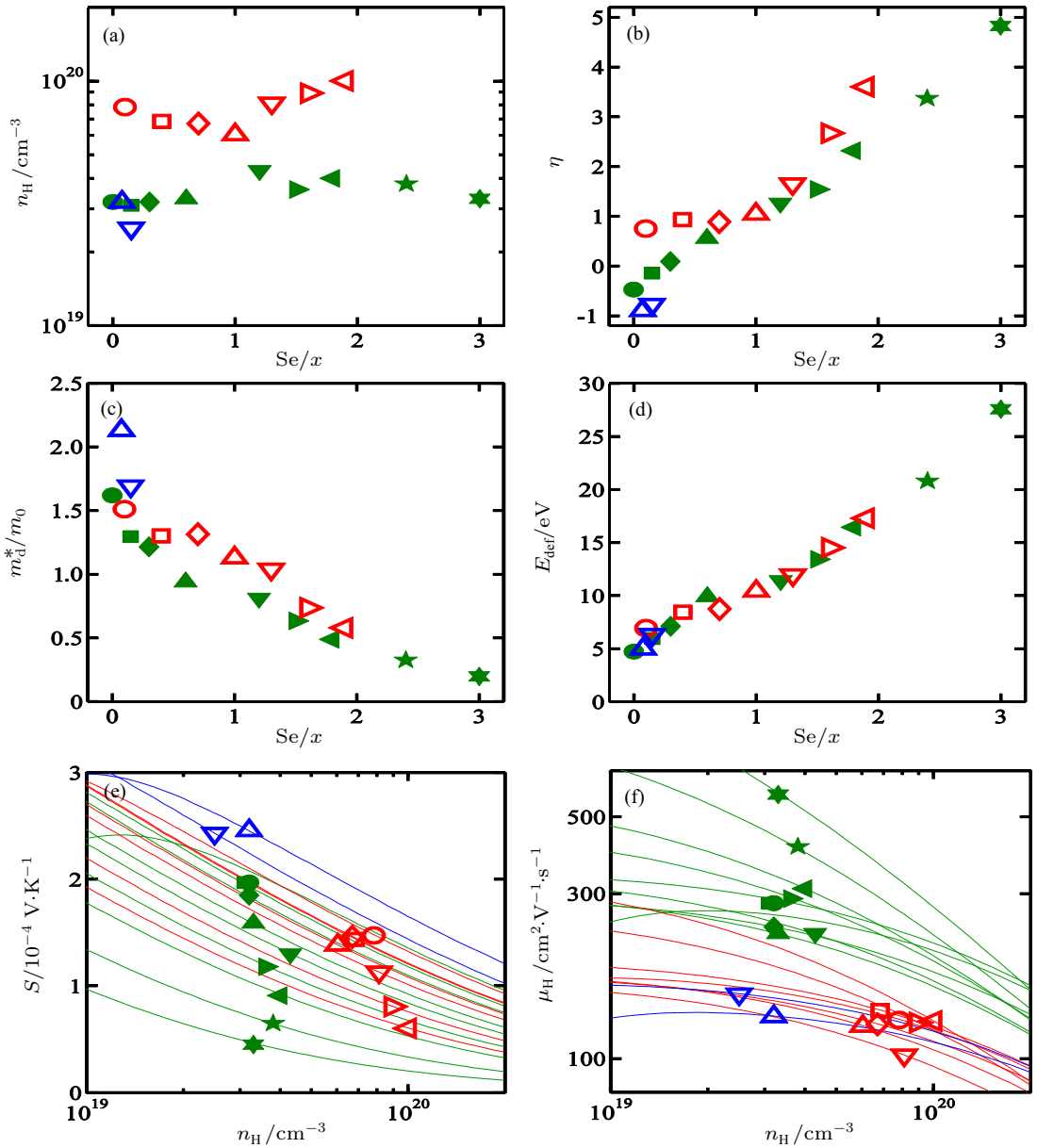


Fig. 18. (color online) The Se content-dependent data points of (a) n_H, (b) determined η, (c) determined m_d^*, and (d) determined E_{def}. The n_H-dependent data points of (e) μ_H, and (f) *S* compared with the theoretical curves of μ_H versus n_H, and *S* versus n_H calculated with the correspondingly determined E_{def}, and m_d^*. In all figures, the solid green data points are from $Bi_2Te_{3-x}Se_x$ ingots doped with I (wt 0.08%),[123] the hollow red data points are from $Bi_2Te_{3-x}Se_x$ processed by BM+HP+HD,[100] and the hollow blue data points are from $Bi_2Te_{3-x}Se_x$ single crystals.[121]

18(c), and 18(d), respectively. On this basis, we calculated the theoretical curves of μ_H and S as a function of n_H for each data point with the correspondingly determined m_d^*, and E_{def}, exhibited in Figs. 18(e) and 18(f), respectively, in which the corresponding data points were also presented. The comparison of data points with the theoretical curves suggests that our determinations for m_d^* and E_{def} are sufficiently precise because the data points locate on the relevant curves, and the values of m_d^* and E_{def} strongly depend on the compositions and the material fabrication methods.

The combination of theoretical curves of μ_H versus n_H and S versus n_H enables to calculate the theoretical curves of $S^2\sigma$ versus n_H, shown in Fig. 19(a), in which the corresponding data points are also plotted. According to our discussion in Section 4, n_H^{opt} mainly depends on m_d^*. To examine the relations between $S^2\sigma$ peak and n_H, figure 19(b) demonstrates the data points of determined m_d^* and n_H for all studied materials, compared with the previously determined curve of m_d^* versus n_H^{opt} from Fig. 8(b). As can be seen, when the data points are located closer to the grey curve in Fig. 19(b), it is more likely for the data points in Fig. 19(a) to approach the peaks of corresponding theoretical curves of $S^2\sigma$ versus n_H. However, the difference of $S^2\sigma$ values for different data points cannot be fully explained by the variation of m_d^*, although small m_d^* could lead to high $S^2\sigma$. For instance, the green hexagon star with m_d^* of $\sim 0.2m_0$ shows $S^2\sigma$ of $\sim 7\times10^{-4}$ W·m^{-1}·K^{-2}, which is much smaller than $S^2\sigma$ of $\sim 6\times10^{-3}$ W·m^{-1}·K^{-2} for the green round disk with m_d^* of $\sim 1.7m_0$. Here, we cannot ascribe the enhanced $S^2\sigma$ to the decreased m_d^*.

Therefore, we should develop new concepts to understand the enhancement in $S^2\sigma$. As reported in our previous study,[38] we defined the λE_{def} (with $\lambda = (m_I^*/m)^{1/2}$), serving as the decoupling factor for S and σ, and we concluded that reducing λE_{def} is the key to enhance $S^2\sigma$, provided that η has been sufficiently optimized. Figure 19(c) shows the data points of determined λE_{def} dependent $S^2\sigma$, compared with the theoretical curves of $S^2\sigma$ versus λE_{def} in the range of 2 eV–6 eV. Note that theoretical curves of $S^2\sigma$ versus λE_{def} were calculated according to the optimal η (η^{opt}). Since η^{opt} is affected by the E_g,[114] for each composition with different E_g, there is a unique theoretical curve of $S^2\sigma$ versus λE_{def}. Considering the small difference of these theoretical curves for various composition, in Fig. 19(c) we only plotted the representative ones for Bi_2Te_3 ingot, $Bi_2Te_{2.4}Se_{0.6}$ ingot, and Bi_2Se_3 ingot. Figure 19(d) presents the data points of λE_{def} against η, compared with the η^{opt} values, indicated by the vertical lines. As can be seen, small λE_{def} indeed results in large $S^2\sigma$ and narrowing the difference between the determined η and the corresponding η^{opt} in Fig. 19(d) allows the data point in Fig. 19(c) to approach the corresponding theoretical curve.

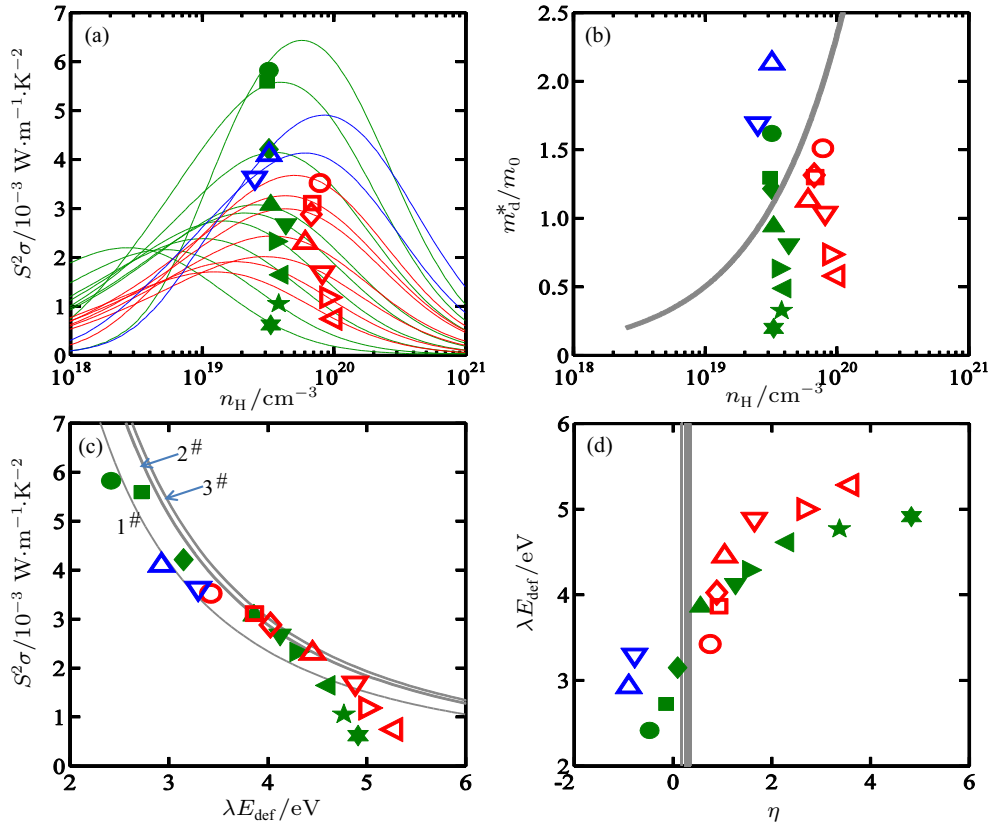


Fig. 19. (color online) (a) Data points of n_H dependent $S^2\sigma$ compared with the theoretical curves of $S^2\sigma$ versus n_H calculated with correspondingly determined E_{def}, and m_d^*. (b) Determined data points of n_H-dependent m_d^* with the grey curve indicating the m_d^* as a function of n_H^{opt}. (c) Data points of λE_{def}-dependent $S^2\sigma$ compared with the theoretical curves of $S^2\sigma$ versus λE_{def} for compositions of Bi_2Te_3 (labeled with 1#), $Bi_2Te_{2.4}Se_{0.6}$ (labeled with 2#) and Bi_2Se_3 (labeled with 3#) calculated with the corresponding η^{opt}. (d) Determined data points of λE_{def} versus η. In all figures, the solid green data points are from $Bi_2Te_{3-x}Se_x$ ingots doped with I (wt 0.08%),[123] the hollow red data points are from $Bi_2Te_{3-x}Se_x$ processed by BM+HP+HD,[100] and the hollow blue data points are from $Bi_2Te_{3-x}Se_x$ single crystals.[121]

Also, we analyzed the p-type BM+HP+HD processed $Bi_xSb_{2-x}Te_3$[100] and the single crystals.[132] Figures 20(a)–20(d) show the n_H, determined η, m_d^*, and E_{def}, respectively. On this basis, we calculated the curves of S and μ_H as a function of n_H over a wide range using the determined parameters, shown in Figs. 20(e) and 20(f), respectively.

Figures 21(a) and 21(d) present the curves of $S^2\sigma$ as a function of n_H, and the determined m_d^* versus n_H. We can observe that when the data point of m_d^* versus n_H is close to the optimal curve of m_d^* versus n_H in Fig. 21(b), the data point of $S^2\sigma$ versus n_H is close to the peak of the corresponding curve of $S^2\sigma$ as a function of n_H. But, although some data points are close to the peak of the corresponding curve of $S^2\sigma$ as a function of n_H, the $S^2\sigma$ could be lower than that for data points deviate from the peak position.

Figures 21(c) and 21(d) present the $S^2\sigma$ as a function of λE_{def}, and λE_{def} versus η, respectively. From which, we can fully understand the reason for enhanced $S^2\sigma$.

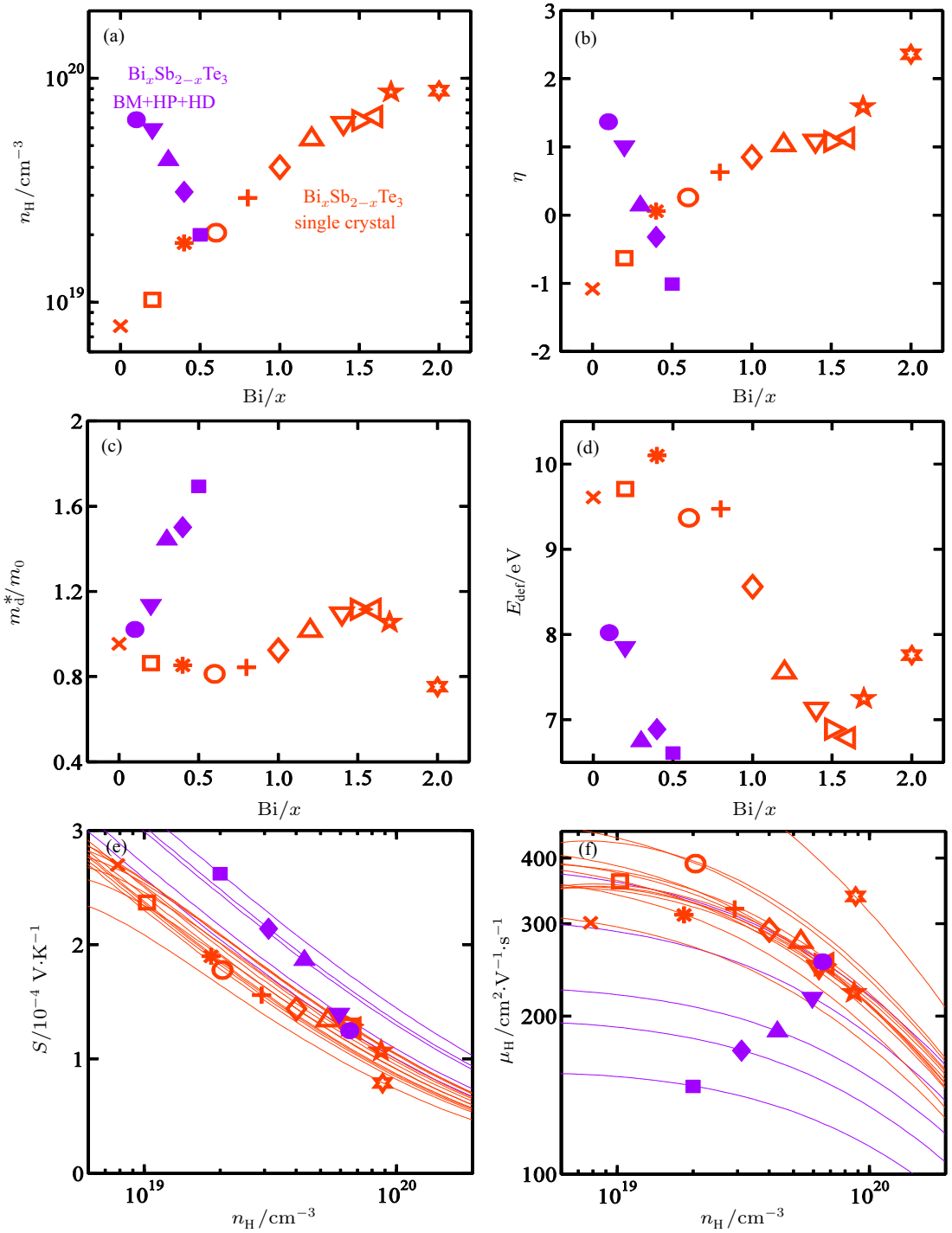


Fig. 20. (color online) (a) n_H of different p-type $Bi_xSb_{2-x}Te_3$. Determined (b) η, (c) m_d^*, and (d) E_{def}. The n_H-dependent data points of (e) μ_H, and (f) S compared with the theoretical curves of μ_H versus n_H, and S versus n_H calculated with the correspondingly determined E_{def}, and m_d^*. In all figures, the solid purple data points correspond to BM+HP+HD processed samples,[100] and the hollowed data points correspond to single crystals.[132]

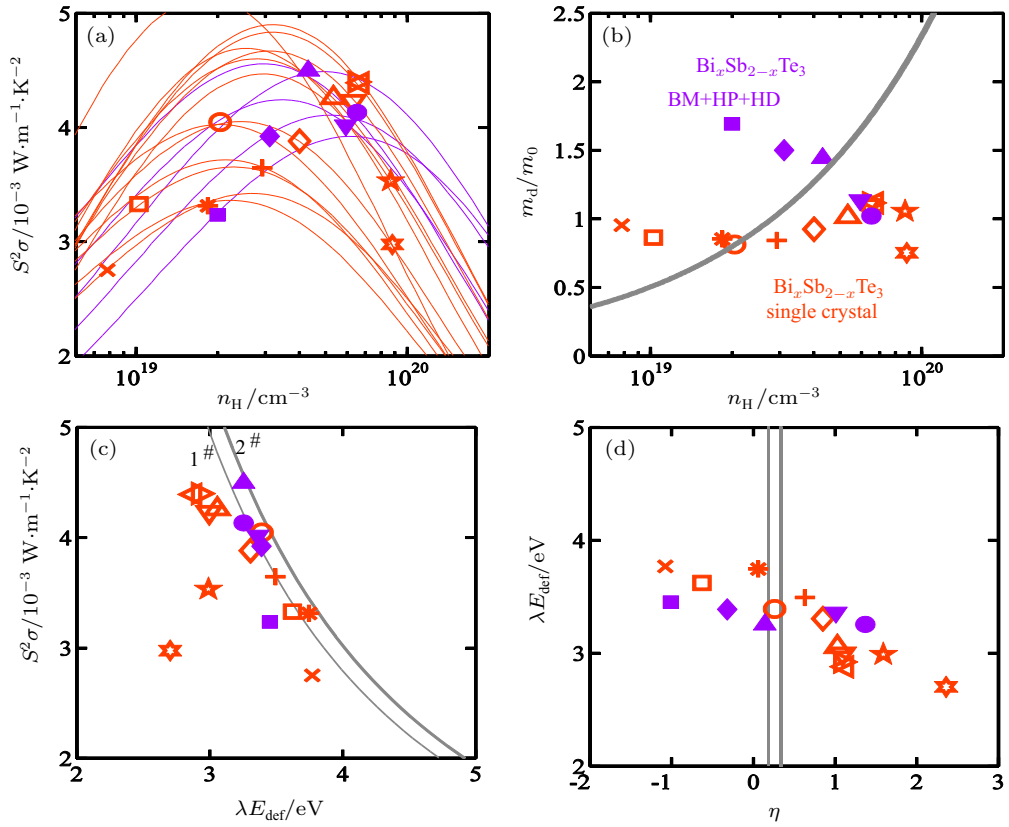


Fig. 21. (color online) (a) Data points of n_H-dependent $S^2\sigma$ compared with the theoretical curves of $S^2\sigma$ versus n_H calculated with correspondingly determined E_{def}, and m_d^*. (b) Determined data points of n_H-dependent m_d^* with the grey curve indicating the m_d^* as a function of n_H^{opt}. (c) Data points of λE_{def} dependent $S^2\sigma$ compared with the theoretical curves of $S^2\sigma$ versus λE_{def} for compositions of Bi_2Te_3 (labeled with $1^{\#}$), and Sb_2Te_3 (labeled with $2^{\#}$) calculated with the corresponding η^{opt}. (d) Determined data points of λE_{def} versus η. In all figures, the solid purple data points correspond to BM+HP+HD processed samples,[100] and the hollowed data points correspond to single crystals.[132]

9. Conclusion and perspectives

In this progress report, we studied the physical fundamentals of thermoelectric effects. While Seebeck effect is the distribution of electrons disturbed by temperature difference, and Peltier effect is the energy exchange between free electrons and the surroundings. We also provided a detailed mathematical process of the derivation of electronic transport coefficients from BTE. On this basis, we performed simulation studies on the effects of materials parameters, m^*, E_g, and E_{def} on these transport coefficients, which provides significant insights into the dependence of thermoelectric properties on materials. We summarized the features of Bi_2Te_3-based thermoelectric, and the correspondingly developed strategies for enhancing the thermoelectric performance. Specifically, owing to the narrow band gap, Bi_2Te_3 families tend to exhibit intensive bipolar conduction. To suppress bipolar conduction, enlarging band gap is required, which is normally achieved by forming ternary phases or doping. Moreover, minor charge carrier filtering can also be applied to suppress the bipolar conduction. Another feather of Bi_2Te_3 is the point defects, which can enhance the mid-frequency phonon scatterings and determine the carrier type as well as carrier concentration. Point defect engineering is widely employed to control the point defects. Finally, caused by the layered structures, Bi_2Te_3 shows anisotropic behavior in terms of the thermoelectric properties along the basal plane and the c axis, which is even stronger in the n-type ones. Therefore, we can observe the n-type $S^2\sigma$ is much lower than that of the p-type. Correspondingly, enhancing the texture of polycrystalline materials is anticipated to improve the thermoelectric performance. Moreover, to understand the strong anisotropic behavior and the reported enhanced thermoelectric performance, we re-analyzed the electronic transport properties of Bi_2Te_3-based thermoelectric materials. The strong anisotropy is found to be caused by the different E_{def} along the a–b basal and c axis. We further analyzed the achieved enhancement in Bi_2Te_3. Based on the modeling studies, we highlight the significance of λE_{def} in enhancing $S^2\sigma$. Reducing λE_{def} is the key to enhance $S^2\sigma$ provided that η has been optimized, which is believed to enlighten the development of high-performance thermoelectric materials.

References

[1] Heremans J P, Jovovic V, Toberer E S, Saramat A, Kurosaki K, Charoenphakdee A, Yamanaka S and Snyder G J 2008 *Science* **321** 554
[2] Lyeo H K, Khajetoorians A A, Shi L, Pipe K P, Ram R J, Shakouri A and Shih C K 2004 *Science* **303** 816
[3] Kim H S, Liu W and Ren Z 2017 *Energy Environ. Sci.* **10** 69
[4] Riffat S B and Ma X L 2003 *Appl. Therm. Eng.* **23** 913
[5] Tritt T M and Subramanian M A 2006 *Mrs. Bull.* **31** 188

[6] Zhu T, Liu Y, Fu C, Heremans J P, Snyder J G and Zhao X 2017 *Adv. Mater.* **29** 1605884
[7] Vining C B 2009 *Nat. Mater.* **8** 83
[8] Ibrahim E A, Szybist J P and Parks J E 2010 *P. I. Mech. Eng. D-J. Automob. Eng.* **224** 1097
[9] Li M, Xu S, Chen Q and Zheng L 2011 *J. Electron. Mater.* **40** 1136
[10] Schierle-Arndt K and Hermes W 2013 *Chem. Unserer. Zeit.* **47** 92
[11] Kraemer D, Jie Q, McEnaney K, Cao F, Liu W, Weinstein L A, Loomis J, Ren Z and Chen G 2016 *Nature Energy* **1** 16153
[12] Kraemer D, Poudel B, Feng H P, Caylor J C, Yu B, Yan X, Ma Y, Wang X, Wang D, Muto A, McEnaney K, Chiesa M, Ren Z and Chen G 2011 *Nat. Mater.* **10** 532
[13] Friedensen V P 1998 *Acta Astronaut.* **42** 395
[14] Yang J H and Caillat T 2006 *Mrs Bull.* **31** 224
[15] O'Brien R C, Ambrosi R M, Bannister N P, Howe S D and Atkinson H V 2008 *J. Nucl. Mater.* **377** 506
[16] Kraemer D, Poudel B, Feng H, Caylor J C, Yu B, Yan X, Ma Y, Wang X, Wang D, Muto A, McEnaney K, Chiesa M, Ren Z and Chen G 2011 *Nat. Mater.* **10** 532
[17] Bahk J H, Fang H, Yazawa K and Shakouri A 2015 *J. Mater. Chem. C* **3** 10362
[18] Hicks L and Dresselhaus M 1993 *Phys. Rev. B* **47** 16631
[19] Harman T C, Taylor P J, Walsh M P and LaForge B E 2002 *Science* **297** 2229
[20] Zhang Q, Liao B, Lan Y, Lukas K, Liu W, Esfarjani K, Opeil C, Broido D, Chen G and Ren Z 2013 *Proc. Natl. Acad. Sci. USA* **110** 13261
[21] Han C, Sun Q, Li Z and Dou S X 2016 *Adv. Energy Mater.* **6** 1600498
[22] Yang H, Bahk J H, Day T, Mohammed A M S, Snyder G J, Shakouri A and Wu Y 2015 *Nano Lett.* **15** 1349
[23] Pei Y, Shi X, LaLonde A, Wang H, Chen L and Snyder G J 2011 *Nature* **473** 66
[24] Liu W, Zhou J, Jie Q, Li Y, Kim H S, Bao J, Chen G and Ren Z 2016 *Energy Environ. Sci.* **9** 530
[25] Liu W, Kim H S, Chen S, Jie Q, Lv B, Yao M, Ren Z, Opeil C P, Wilson S, Chu C W and Ren Z 2015 *Proc. Natl. Acad. Sci. USA* **112** 3269
[26] Yan J, Gorai P, Ortiz B, Miller S, Barnett S A, Mason T, Stevanovic V and Toberer E S 2015 *Energy Environ. Sci.* **8** 983
[27] Hong M, Chen Z G, Pei Y, Yang L and Zou J 2016 *Phys. Rev. B* **94** 161201
[28] Zhao L, Lo S H, Zhang Y, Sun H, Tan G, Uher C, Wolverton C, Dravid V P and Kanatzidis M G 2014 *Nature* **508** 373
[29] Yang L, Chen Z G, Han G, Hong M, Zou Y and Zou J 2015 *Nano Energy* **16** 367
[30] Liu H, Shi X, Xu F, Zhang L, Zhang W, Chen L, Li Q, Uher C, Day T and Snyder G J 2012 *Nat. Mater.* **11** 422
[31] Dresselhaus M S, Chen G, Tang M Y, Yang R G, Lee H, Wang D Z, Ren Z F, Fleurial J P and Gogna P 2007 *Adv. Mater.* **19** 1043
[32] Pichanusakorn P and Bandaru P 2010 *Mat. Sci. Eng. R.* **67** 19
[33] Hong M, Chen Z G, Yang L, Chasapis T C, Kang S D, Zou Y, Auchterlonie G J, Kanatzidis M G, Snyder G J and Zou J 2017 *J. Mater. Chem. A* **5** 10713
[34] Kanatzidis M G 2010 *Chem. Mater.* **22** 648
[35] Son J S, Choi M K, Han M K, Park K, Kim J Y, Lim S J, Oh M, Kuk Y, Park C, Kim S J and Hyeon T 2012 *Nano Lett.* **12** 640
[36] Zhang G, Kirk B, Jauregui L A, Yang H, Xu X, Chen Y P and Wu Y 2012 *Nano Lett.* **12** 56
[37] Hong M, Chasapis T C, Chen Z G, Yang L, Kanatzidis M G, Snyder G J and Zou J 2016 *ACS Nano* **10** 4719
[38] Hong M, Chen Z G, Yang L and Zou J 2016 *Nano Energy* **20** 144
[39] Zhang X D and Xie Y 2013 *Chem. Soc. Rev.* **42** 8187
[40] Fang H, Feng T, Yang H, Ruan X and Wu Y 2013 *Nano Lett.* **13** 2058
[41] Fang H, Yang H and Wu Y 2014 *Chem. Mater.* **26** 3322
[42] Hong M, Chen Z G, Yang L and Zou J 2016 *Nanoscale* **8** 8681
[43] Chen Z, Jian Z, Li W, Chang Y, Ge B, Hanus R, Yang J, Chen Y, Huang M, Snyder G J and Pei Y 2017 *Adv. Mater.* **29** 1606768
[44] Chen Z, Ge B, Li W, Lin S, Shen J, Chang Y, Hanus R, Snyder G J and Pei Y 2017 *Nat. Commun.* **8** 13828
[45] Tan G, Zhao L D and Kanatzidis M G 2016 *Chem. Rev.*
[46] Hong M, Chen Z G, Yang L, Liao Z M, Zou Y C, Chen Y H, Matsumura S and Zou J 2018 *Adv. Energy Mater.* **8** 1702333
[47] Hong M, Chen Z G, Yang L, Zou Y C, Dargusch M S, Wang H and Zou J 2018 *Adv. Mater.* **30** 1705942
[48] Biswas K, He J, Blum I D, Wu C I, Hogan T P, Seidman D N, Dravid V P and Kanatzidis M G 2012 *Nature* **489** 414
[49] Sootsman J R, Chung D Y and Kanatzidis M G 2009 *Angew. Chem. Int. Ed.* **48** 8616
[50] Wu H J, Zhao L D, Zheng F S, Wu D, Pei Y L, Tong X, Kanatzidis M G and He J Q 2014 *Nat. Commun.* **5** 5515
[51] Wu H, Zheng F, Wu D, Ge Z H, Liu X and He J 2015 *Nano Energy* **13** 626
[52] Wu H, Carrete J, Zhang Z, Qu Y, Shen X, Wang Z, Zhao L D and He J 2014 *NPG Asia Mater.* **6** e108
[53] He J, Kanatzidis M G and Dravid V P 2013 *Materials Today* **16** 166
[54] Tritt T M 1999 *Science* **283** 804
[55] Joshi G, Lee H, Lan Y, Wang X, Zhu G, Wang D, Gould R W, Cuff D C, Tang M Y, Dresselhaus M S, Chen G and Ren Z 2008 *Nano Lett.* **8** 4670
[56] Moshwan R, Yang L, Zou J and Chen Z G 2017 *Adv. Funct. Mater.* **27** 1703278
[57] Tan G, Zhao L D, Shi F, Doak J W, Lo S H, Sun H, Wolverton C, Dravid V P, Uher C and Kanatzidis M G 2014 *J. Am. Chem. Soc.* **136** 7006
[58] Tan G, Shi F, Hao S, Chi H, Zhao L D, Uher C, Wolverton C, Dravid V P and Kanatzidis M G 2015 *J. Am. Chem. Soc.* **137** 5100
[59] Tan G, Shi F, Hao S, Chi H, Bailey T P, Zhao L D, Uher C, Wolverton C, Dravid V P and Kanatzidis M G 2015 *J. Am. Chem. Soc.* **137** 11507
[60] Tan G, Shi F, Doak J W, Sun H, Zhao L D, Wang P, Uher C, Wolverton C, Dravid V P and Kanatzidis M G 2015 *Energy Environ. Sci.* **8** 267
[61] Yang L, Chen Z G, Dargusch M S and Zou J 2018 *Adv. Energy Mater.* **8** 1701797
[62] Zhao L D, Tan G, Hao S, He J, Pei Y, Chi H, Wang H, Gong S, Xu H, Dravid V P, Uher C, Snyder G J, Wolverton C and Kanatzidis M G 2016 *Science* **351** 141
[63] Peng K, Lu X, Zhan H, Hui S, Tang X, Wang G, Dai J, Uher C, Wang G and Zhou X 2016 *Energy Environ. Sci.* **9** 454
[64] Bell L E 2008 *Science* **321** 1457
[65] DiSalvo F J 1999 *Science* **285** 703
[66] Chen Z G, Han G, Yang L, Cheng L and Zou J 2012 *Prog. Nat. Sci.* **22** 535
[67] Wang H, Pei Y, LaLonde A D and Snyder G J 2012 *Proc. Natl. Acad. Sci. USA* **109** 9705
[68] Tang Y, Gibbs Z M, Agapito L A, Li G, Kim H S, Nardelli M B, Curtarolo S and Snyder G J 2015 *Nat. Mater.* **14** 1223
[69] Wang X W, Lee H, Lan Y C, Zhu G H, Joshi G, Wang D Z, Yang J, Muto A J, Tang M Y, Klatsky J, Song S, Dresselhaus M S, Chen G and Ren Z F 2008 *Appl. Phys. Lett.* **93** 193121
[70] Poudel B, Hao Q, Ma Y, Lan Y, Minnich A, Yu B, Yan X, Wang D, Muto A, Vashaee D, Chen X, Liu J, Dresselhaus M S, Chen G and Ren Z 2008 *Science* **320** 634
[71] Fu C, Zhu T, Liu Y, Xie H and Zhao X 2015 *Energy Environ. Sci.* **8** 216
[72] Yang J 2007 *J. Electron. Mater.* **36** 703
[73] Zhang X and Zhao L D 2015 *Journal of Materiomics* **1** 92
[74] Wood C 1988 *Rep. Prog. Phys.* **51** 459
[75] Beekman M and Nolas G S 2008 *J. Mater. Chem.* **18** 842
[76] Shakouri A 2005 *IEEE Thermoelectric, thermionic and thermophotovoltaic energy conversion.*, p. 495
[77] Mahan G D 2005 *Thermoelectric Effect. In Encyclopedia of Condensed Matter Physics*, Editors-in-Chief: Franco B, Eds. Gerald L L, Peter W (Oxford: Elsevier) p. 180
[78] Dimitrijev S 2006 *Principles of semiconductor devices* (New York: Oxford University Press)
[79] Hamaguchi C *Basic Semiconductor Physics*
[80] Ioffe A F 1960 *Physics of Semiconductors* (Academic Press)
[81] Vesely F 1995 *Computational Physics: an introduction* (New York: Plenum)
[82] Mohamad A A 2011 *Lattice Boltzmann Method* (Dordrecht: Springer)
[83] Nolas G S, Sharp J and Goldsmid H J 2001 *Thermoelectrics: Basic Principles and New Materials Developments* (Berlin: Springer)
[84] Ashcroft N W and Mermin N D 1976 *Holt, Rinehart and Winston* (New York)
[85] Fistul I V 1969 *Heavily Doped Semiconductors* (New York: Springer)
[86] Zhao L, Lo S H, He J, Li H, Biswas K, Androulakis J, Wu C I, Hogan T P, Chung D Y, Dravid V P and Kanatzidis M G 2011 *J. Am. Chem. Soc.* **133** 20476

[87] Heremans J P, Thrush C M and Morelli D T 2004 *Phys. Rev. B* **70** 115334
[88] Huang B L and Kaviany M 2008 *Phys. Rev. B* **77** 125209
[89] Faleev S V and Léonard F 2008 *Phys. Rev. B* **77** 214304
[90] Ravich Y I, Efimova B A and Smirnov I A 1970 *Semiconducting Lead Chalcogenides* (Plenum Press)
[91] Wu D, Zhao L D, Hao S Q, Jiang Q K, Zheng F S, Doak J W, Wu H J, Chi H, Gelbstein Y, Uher C, Wolverton C, Kanatzidis M and He J Q 2014 *J. Am. Chem. Soc.* **136** 11412
[92] Chasapis T C, Lee Y, Hatzikraniotis E, Paraskevopoulos K M, Chi H, Uher C and Kanatzidis M G 2015 *Phys. Rev. B* **91** 085207
[93] Chen C L, Wang H, Chen Y Y, Day T and Snyder G J 2014 *J. Mater. Chem. A* **2** 11171
[94] Wang H, LaLonde A D, Pei Y and Snyder G J 2013 *Adv. Funct. Mater.* **23** 1586
[95] Mishra S K, Satpathy S and Jepsen O 1997 *J. Phys.: Condens. Matter* **9** 461
[96] Qiu B and Ruan X 2009 *Phys. Rev. B* **80** 165203
[97] Yavorsky B Y, Hinsche N F, Mertig I and Zahn P 2011 *Phys. Rev. B* **84** 165208
[98] Richter W, Kohler H and Becker C R 1977 *Phys. Status Solidi B* **84** 619
[99] Hu L, Wu H, Zhu T, Fu C, He J, Ying P and Zhao X 2015 *Adv. Energy Mater.* **5** 1500411
[100] Hu L, Zhu T, Liu X and Zhao X 2014 *Adv. Funct. Mater.* **24** 5211
[101] Prokofieva L V, Pshenay-Severin D A, Konstantinov P P and Shabaldin A A 2009 *Semiconductors* **43** 973
[102] Zhao L D, Zhang B P, Li J F, Zhang H L and Liu W S 2008 *Solid State Sci.* **10** 651
[103] Xie W, Tang X, Yan Y, Zhang Q and Tritt T M 2009 *Appl. Phys. Lett.* **94** 102111
[104] Mehta R J, Zhang Y, Karthik C, Singh B, Siegel R W, Borca-Tasciuc T and Ramanath G 2012 *Nat. Mater.* **11** 233
[105] Soni A, Shen Y, Yin M, Zhao Y, Yu L, Hu X, Dong Z, Khor K A, Dresselhaus M S and Xiong Q 2012 *Nano Lett.* **12** 4305
[106] Soni A, Zhao Y Y, Yu L G, Aik M K K, Dresselhaus M S and Xiong Q H 2012 *Nano Lett.* **12** 1203
[107] Scheele M, Oeschler N, Veremchuk I, Reinsberg K G, Kreuziger A M, Kornowski A, Broekaert J, Klinke C and Weller H 2010 *ACS Nano* **4** 4283
[108] Min Y, Roh J W, Yang H, Park M, Kim S I, Hwang S, Lee S M, Lee K H and Jeong U 2013 *Adv. Mater.* **25** 1425
[109] Min Y, Park G, Kim B, Giri A, Zeng J, Roh J W, Kim S I, Lee K H and Jeong U 2015 *ACS Nano* **9** 6843
[110] Suh D, Lee S, Mun H, Park S H, Lee K H, Wng Kim S, Choi J Y and Baik S 2015 *Nano Energy* **13** 67
[111] Zhang Y, Day T, Snedaker M L, Wang H, Krämer S, Birkel C S, Ji X, Liu D, Snyder G J and Stucky G D 2012 *Adv. Mater.* **24** 5065
[112] Zhang Y, Wang H, Kräemer S, Shi Y, Zhang F, Snedaker M, Ding K, Moskovits M, Snyder G J and Stucky G D 2011 *ACS Nano* **5** 3158
[113] Sun Y, Cheng H, Gao S, Liu Q, Sun Z, Xiao C, Wu C, Wei S and Xie Y 2012 *J. Am. Chem. Soc.* **134** 20294
[114] Hong M, Chen Z G, Yang L, Han G and Zou J 2015 *Adv. Electron. Mater.* **1** 1500025
[115] Mehta R J, Zhang Y, Zhu H, Parker D S, Belley M, Singh D J, Ramprasad R, Borca-Tasciuc T and Ramanath G 2012 *Nano Lett.* **12** 4523
[116] Yu F, Xu B, Zhang J, Yu D, He J, Liu Z and Tian Y 2012 *Mater. Res. Bull.* **47** 1432
[117] Kang Y, Zhang Q, Fan C, Hu W, Chen C, Zhang L, Yu F, Tian Y and Xu B 2017 *J. Alloys Compd.* **700** 223
[118] Ma Y, Hao Q, Poudel B, Lan Y C, Yu B, Wang D Z, Chen G and Ren Z F 2008 *Nano Lett.* **8** 2580
[119] Yan X, Poudel B, Ma Y, Liu W S, Joshi G, Wang H, Lan Y, Wang D, Chen G and Ren Z F 2010 *Nano Lett.* **10** 3373
[120] Shen J J, Zhu T J, Zhao X B, Zhang S N, Yang S H and Yin Z Z 2010 *Energy Environ. Sci.* **3** 1519
[121] Carle M, Pierrat P, Lahalle-Gravier C, Scherrer S and Scherrer H 1995 *J. Phys. Chem. Solids* **56** 201
[122] Liu W S, Zhang Q, Lan Y, Chen S, Yan X, Zhang Q, Wang H, Wang D, Chen G and Ren Z 2011 *Adv. Energy Mater.* **1** 577
[123] Wang S, Tan G, Xie W, Zheng G, Li H, Yang J and Tang X 2012 *J. Mater. Chem.* **22** 20943
[124] Minnich A J, Dresselhaus M S, Ren Z F and Chen G 2009 *Energy Environ. Sci.* **2** 466
[125] Wang S, Yang J, Toll T, Yang J, Zhang W and Tang X 2015 *Sci. Rep.* **5** 10136
[126] Goldsmid H J and Sharp J W 1999 *J. Electron. Mater.* **28** 869
[127] Gibbs Z M, Kim H S, Wang H and Snyder G J 2015 *Appl. Phys. Lett.* **106** 022112
[128] Starý Z, Horák J, Stordeur M and Stölzer M 1988 *J. Phys. Chem. Solids* **49** 29
[129] Slack G A 1995 "New Materials and Performance Limits for Thermoelectric Cooling", *in CRC Handbook of Thermoelectrics*, Rowe D M, ed. (CRC Press) p. 407
[130] Dean J A and Lange N A 1999 *Lange's Handbook of Chemistry* (New York: McGraw-Hill) Vol. 15
[131] Ortiz B R, Peng H, Lopez A, Parilla P A, Lany S and Toberer E S 2015 *Phys. Chem. Chem. Phys.* **17** 19410
[132] Caillat T, Carle M, Pierrat P, Scherrer H and Scherrer S 1992 *J. Phys. Chem. Solids* **53** 1121
[133] Min Y, Moon G D, Kim B S, Lim B, Kim J S, Kang C Y and Jeong U 2012 *J. Am. Chem. Soc.* **134** 2872
[134] Wiese J R and Muldawer L 1960 *J. Phys. Chem. Solids* **15** 13
[135] Kutasov V A, Lukyanova L N and Vedernikov M V 2005 "Shifting the Maximum Figure-of-Merit of (Bi, Sb)2(Te, Se)3 Thermoelectrics to Lower Temperatures", *in Thermoelectrics Handbook*, Rowe D M, ed. (CRC Press) p. 37
[136] Greenaway D L and Harbeke G 1965 *J. Phys. Chem. Solids* **26** 1585
[137] Sehr R and Testardi L R 1962 *J. Phys. Chem. Solids* **23** 1219
[138] Xiao C, Li Z, Li K, Huang P and Xie Y 2014 *Acc. Chem. Res.* **47** 1287
[139] Sun L P, Lin Z P, Peng J, Weng J, Huang Y Z and Luo Z Q 2014 *Sci. Rep.* **4** 4794
[140] Zhou G and Wang D 2015 *Sci. Rep.* **5** 8099
[141] Sakamoto Y, Hirahara T, Miyazaki H, Kimura S I and Hasegawa S 2010 *Phys. Rev. B* **81** 165432
[142] Scanlon D O, King P D C, Singh R P, de la Torre A, Walker S M, Balakrishnan G, Baumberger F and Catlow C R A 2012 *Adv. Mater.* **24** 2154
[143] Cheng L, Chen Z G, Yang L, Han G, Xu H Y, Snyder G J, Lu G Q and Zou J 2013 *J. Phys. Chem. C* **117** 12458
[144] Yang L, Chen Z G, Hong M, Han G and Zou J 2015 *ACS Appl. Mater. Interf.* **7** 23694
[145] Hu L P, Zhu T J, Wang Y G, Xie H H, Xu Z J and Zhao X B 2014 *NPG Asia Mater.* **6** e88
[146] Birkholz U 1958 "Untersuchung der Intermetallischen Verbindung Bi_2Te_3 Sowie der Festen Lösungen $Bi_{2-x}Sb_xTe_3$ und $Bi_2Te_{3-x}Se_x$ Hinsichtlich Ihrer Eignung als Material für Halbleiter-Thermoelemente", *Zeitschrift für Naturforschung A*, Vol. 13, p. 780
[147] Zhao L D, Zhang B P, Liu W S and Li J F 2009 *J. Appl. Phys.* **105** 023704
[148] Ge Z H, Zhao L D, Wu D, Liu X, Zhang B P, Li J F and He J 2016 *Materials Today* **19** 227
[149] Shen J J, Zhu T J, Zhao X B, Zhang S N, Yang S H and Yin Z Z 2010 *Energy Environ. Sci.* **3** 1519
[150] Xiu F, He L, Wang Y, Cheng L, Chang L T, Lang M, Huang G, Kou X, Zhou Y, Jiang X, Chen Z, Zou J, Shailos A and Wang K L 2011 *Nat. Nano* **6** 216
[151] Hong M, Chen Z G, Yang L and Zou J 2016 *Nanoscale* **8** 8681
[152] Mi J L, Lock N, Sun T, Christensen M, Sondergaard M, Hald P, Hng H H, Ma J and Iversen B B 2010 *ACS Nano* **4** 2523
[153] Lu W G, Ding Y, Chen Y X, Wang Z L and Fang J Y 2005 *J. Am. Chem. Soc.* **127** 10112
[154] Zhang Y, Hu L P, Zhu T J, Xie J and Zhao X B 2013 *Cryst. Growth Des.* **13** 645
[155] Fu J, Song S, Zhang X, Cao F, Zhou L, Li X and Zhang H 2012 *CrystEngComm* **14** 2159
[156] Son J H, Oh M W, Kim B S, Park S D, Min B K, Kim M H and Lee H W 2013 *J. Alloys Compd.* **566** 168
[157] Zheng Y, Zhang Q, Su X, Xie H, Shu S, Chen T, Tan G, Yan Y, Tang X, Uher C and Snyder G J 2015 *Adv. Energy Mater.* **5** 1401391
[158] Ivanova L D, Petrova L I, Granatkina Y V, Leontyev V G, Ivanov A S, Varlamov S A, Prilepo Y P, Sychev A M, Chuiko A G and Bashkov I V 2013 *Inorg. Mater.* **49** 120
[159] Ivanova L D, Petrova L I, Granatkina Y V, Kichik S A, Marakushev I S and Mel'nikov A A 2015 *Inorg. Mater.* **51** 741
[160] Kim S I, Lee K H, Mun H A, Kim H S, Hwang S W, Roh J W, Yang D J, Shin W H, Li X S, Lee Y H, Snyder G J and Kim S W 2015 *Science* **348** 109
[161] Zhao L D, Dravid V P and Kanatzidis M G 2014 *Energy Environ. Sci.* **7** 251